Mathematics

AIMS Mathematics, 10(4): 9563−9594.
DOI: 10.3934/math.2025441
Received: 07 January 2025
Revised: 29 March 2025
Accepted: 15 April 2025
Published: 25 April 2025

https://www.aimspress.com/journal/Math

Research article

Analysis of the radiated ternary hybrid nanofluid flow containing TiO_2, $CoFe_2O_4$ and MgO nanoparticles past a bi-directional extending sheet using thermal convective and velocity slip conditions

Humaira Yasmin[1,2,*], Rawan Bossly[3], Fuad S. Alduais[4], Afrah Al-Bossly[4] and Anwar Saeed[5]

[1] Department of Basic Sciences, General Administration of Preparatory Year, King Faisal University, P.O. Box 400, Al Ahsa 31982, Saudi Arabia
[2] Department of Mathematics and Statistics, College of Science, King Faisal University, P.O. Box 400, Al Ahsa 31982, Saudi Arabia
[3] Department of Mathematics, College of Science, Jazan University, Jazan 82817, Saudi Arabia
[4] Department of Mathematics, College of Science and Humanities in Al-Kharj, Prince Sattam bin Abdulaziz University, Al-Kharj 11942, Saudi Arabia
[5] Independent Researcher, Peshawar, 25000, Khyber Pakhtunkhwa, Pakistan

* **Correspondence:** Email: hhassain@kfu.edu.sa.

Abstract: We examined ternary hybrid Carreau nanofluid flow on a porous bi-directional elongating sheet. The nanoparticles of TiO_2, $CoFe_2O_4$, and MgO were mixed with water to get a ternary hybrid nanofluid. The flow was influenced by slip conditions of velocities along the x- and y-axes. The impacts of thermal- and space-dependent heat sources, thermal radiation, viscous dissipation, and Joule heating were used in this study. Moreover, magnetic effects were used along the z-axis, which was normal to the flow direction. The major equations were solved using the homotopy analysis method (HAM) in dimensionless form. As an outcome of this study, we discovered that with progression in velocity slip factors along x- and y-axes, magnetic factor, porosity factor, and local Weissenberg number, there was a reduction in primary and secondary velocities. With an upsurge in the stretching ratio factor, there was a reduction in primary flow and augmentation in secondary flow. Thermal distribution was augmented with the surge in thermal Biot number, thermal-dependent heat source factor, magnetic factor, space-dependent heat source parameter, radiation factor, and Eckert numbers along primary and secondary directions. The skin friction coefficients have augmented with growth in magnetic factor, porosity factor, and velocity slip factors along the x- and y-axes. The Nusselt number escalated with a

surge in radiation factor, space-dependent heat source factor, thermal-dependent heat source factor, and Eckert numbers along x- and y-axes. Our results were validated through comparative analysis by matching our results with established data. A fine agreement was noticed among all the results. Our findings benefit aerospace, biomedical, and electronics industries by improving thermal management in porous media. Magnetic and slip conditions aid in advanced manufacturing, while enhanced Nusselt numbers support efficient heat exchanger design.

Keywords: ternary hybrid nanofluid; Carreau nanofluid; thermal radiation; heat source; viscous dissipation; Joule heating; slip conditions
Mathematics Subject Classification: 76A02, 76D05, 65L10

Nomenclature

Symbol	Name	Symbol	Name
u, v, w	Velocity components $\left[m.s^{-1}\right]$	x, y, z	Coordinate axis $\left[m\right]$
u_w, v_w	Velocities along *x- and y*-directions $\left[m.s^{-1}\right]$	b	Constant
c	Constant	T_w	Surface temperature $\left[K\right]$
T_f	Fluid temperature $\left[K\right]$	T_∞	Free-stream temperature $\left(K\right)$
B_0	Intensity of magnetic field $\left[A.m^{-1}\right]$	σ	Electrical conductivity $\left[S.m^{-1}\right]$
ν	Kinematic viscosity $\left[m^2.s^{-1}\right]$	μ	Dynamic viscosity $\left[kg.m^{-1}.s^{-1}\right]$
K	Porosity coefficient $\left[m^2\right]$	δ	Material constant
n	Power-law index	k	Thermal conductivity $\left[W.m^{-1}.K^{-1}\right]$
k^*	Mean absorption coefficient	σ^*	Stefan–Boltzmann constant $\left[W.m^{-2}.K^{-4}\right]$
C_p	Specific heat $\left[J.kg.K^{-1}\right]$	Q_S	Space-dependent heat source coefficient $\left[W.m^{-3}.K^{-1}\right]$
Q_T	Thermal-dependent heat source coefficient $\left[W.m^{-3}.K^{-1}\right]$	A_1^*	Coefficient of velocity slip along the *x*-direction
A_2^*	Coefficient of velocity slip along the *y*-direction	X	Nanoparticle volume fraction

1. Introduction

Nanofluid flow designates the motion of a base fluid comprising nanoparticles (with a size of 1−100 nm). These nanoparticles enhance thermal conductivity, improve heat transfer rates, and reduce viscosity effects, as revealed first by Choi and Eastman [1]. Nanofluids demonstrate superior convective heat transfer, making them ideal for cooling systems, microelectronics, and biomedical devices. Ali et al. [2] investigated numerically micro-polar nanofluid flow on a surface. Galal et al. [3]

deliberated on MHD nanoliquid flow on a surface with inclined magnetic effects. Hybrid nanofluids consist of two diverse kinds of nanoparticles dispersed in a base fluid, offering improved thermal properties compared to single-nanoparticle nanofluids, as highlighted by Algehyne et al. [4]. These fluids exhibit enhanced thermal conductance and stability due to synergistic effects [5,6]. The study of hybrid nanofluid flow involves analyzing their rheological behavior, stability, and heat transfer characteristics, which depend on nanoparticles' shape, size, volume fraction, temperature, and flow conditions, including laminar or turbulent regimes. Ternary hybrid nanofluids contain three unlike nanoparticles mixed in a base fluid, offering even greater thermal and mechanical advantages than hybrid nanofluids. Guedri et al. [7] explored that these fluids exhibit superior heat transfer performance, enhanced stability, and reduced viscosity compared to single and hybrid nanofluids. Researchers have focused on optimizing these fluids for maximum efficiency in applications like nuclear cooling, aerospace, and advanced energy systems [8]. Nanofluids, hybrid nanofluids, and ternary hybrid nanofluids significantly impact velocity and temperature profiles in fluid dynamics. Shah et al. [9] revealed that the addition of nanoparticles generally increases viscosity, which can reduce velocity due to higher resistance. However, thermal conductivity improves, leading to higher heat transfer rates and reduced temperature gradients. In hybrid and ternary hybrid nanofluids, the combined properties of different nanoparticles enhance energy transport, further increasing thermal efficiency. Near heated surfaces, temperature profiles rise due to improved heat absorption. Advanced nanofluids offer optimized thermal and flow performance in engineering applications. Rabby et al. [10] discussed the ternary hybrid nanofluid flow by discussing its preparation, properties, and stability.

Fluid flow with thermal radiation is an interesting phenomenon where heat transfer occurs due to convective and radiative effects. In many engineering applications, like aerospace, nuclear reactors, and industrial furnaces, thermal radiation plays a vital role in influencing the temperature distribution within a flowing fluid [11]. When a fluid flows past a heated surface, heat is transferred through conduction at the interface, convection within the bulk fluid, and radiation if the temperature is sufficiently high. The governing equations for such flows include the energy equation accounting for convective and radiative heat transfer and the radiative transfer equation, which describes how radiation propagates through a medium. Anwar et al. [12] studied thermally radiative effects in the existence of a thermal-based source on nanofluid flow on a surface. Sarfraz et al. [13] investigated that the existence of radiation alters the temperature gradients in the fluid, which affects its density, viscosity, and overall flow characteristics. Nayfeh et al. [14] highlighted that for optically thin fluids, radiation directly influences the temperature field without significant absorption, whereas in optically thick fluids, radiation is absorbed and re-emitted multiple times, leading to more uniform temperature distributions. In engineering applications, thermal radiation is vital for designing efficient cooling systems, improving thermal insulation, and predicting heat transfer rates accurately [15]. Thermal radiation significantly alters thermal profiles by introducing additional heat transfer pathways. In high-temperature flows, radiation reduces steep temperature gradients, leading to more uniform temperature distributions. Sohail et al. [16] discussed thermal radiative effects on nanofluid flow past a disk. The study of fluid flow with thermal radiation is particularly important in high-temperature industrial processes and fire safety engineering, where radiation significantly influences heat transfer and fluid motion [17]. Bilal and Riaz [18] studied Williamson fluid flow on a stratified surface with thermal radiative effects by implementing a machine learning methodology. In industrial applications, radiation modifies cooling rates, affecting material properties. These impacts help engineers design better thermal management systems in reactors, combustion chambers, and space applications where radiative effects dominate heat transfer processes.

Fluid flow with a heat source is a vital phenomenon in engineering and natural systems, involving

fluid motion while heat is added or removed. This process is mathematically governed by a specific term in the energy equation for heat transfer. Heat sources can be internal (like chemical reactions or electrical heating) or external (like radiative or convective heating). Ali et al. [19] investigated that the existence of a heat source alters the temperature distribution in the fluid, leading to variations in density and viscosity. These variations can induce buoyancy-driven flow, also known as natural convection, where hotter fluid rises and cooler fluid sinks, forming complex circulation patterns. Jalili et al. [20] discussed thermally the MHD Jeffery fluid flow on a surface with a heat source and chemically reactive effects. Alqawasmi et al. [21] inspected ternary hybrid nanofluid flow on a sheet with the effects of a heat source. The interaction between flow and heat influences velocity fields, pressure distribution, and turbulence characteristics. Madhukesh et al. [22] examined the ternary hybrid nanoliquid flow computationally through a conduit with impacts of heat sink/source. High heat fluxes can result in thermal boundary layers, affecting heat transfer efficiency. In industrial applications, such flows are found in cooling systems, nuclear reactors, and combustion chambers [23]. Vinodkumar Reddy [24] discussed the effects of heat source on stagnant point MHD fluid flow through a permeable medium subject to chemically reactive effects. Abbas et al. [25] emphasized that the existence of a heat source significantly alters thermal profiles by introducing temperature gradients that drive heat transfer. In steady-state conditions, temperature increases near the source and gradually decreases outward, forming a thermal boundary layer. Variations in the thermal profile influence system efficiency, material stress, and energy losses in industrial and natural applications. Swain et al. [26] discussed numerically three-dimensional Maxwell nanoparticle flow on a permeable elongated sheet with effects of heat sink/source.

Viscous dissipation in fluid flow describes the alteration of mechanical to thermal energy. This occurs because viscosity causes energy loss in the form of heat. The effect is particularly significant in high-speed flows, microfluidic systems, and flows with high shear rates, like those in lubrication, polymer processing, and geophysical applications [27]. The governing equation for heat transfer with viscous dissipation is derived from the energy equation, which includes a term accounting for the heat generated by shear stresses. Mathematically, this is expressed as the dissipation function, which depends on velocity gradients and viscosity. Khedher et al. [28] scrutinized the dissipative effects on EMHD fluid flow along a horizontal circular cylinder. Rehman et al. [29] discussed dissipative fluid flow on an extending sheet by computing the analytical solution. The significance of viscous dissipation varies depending on the flow regime, fluid properties, and boundary conditions [30]. In laminar flows, dissipation effects are moderate, while in turbulent flows, they become more intense due to chaotic fluid motion. Li et al. [31] explored that viscous dissipation alters thermal profiles by introducing additional heat sources within the fluid, affecting temperature gradients and heat transfer rates. In shear-dominated flows, this can lead to higher core temperatures, flattening thermal profiles. In microchannels, where heat transfer mechanisms differ from macroscale systems, viscous dissipation becomes a crucial factor in temperature distribution. Additionally, in natural convection, dissipation can either enhance or suppress buoyancy-driven flows depending on whether the added heat increases or decreases the fluid density gradients. Viscous dissipation plays a main role in various uses like cooling of electronic components, biological fluid mechanics, and industrial heat exchangers [32]. Abid and Hasnain [33] used viscous dissipative effects on Casson fluid flow over a curved artery surface and highlighted that proper analysis of this effect ensures optimized thermal management and prevents overheating in high-performance systems.

Fluid flow with Joule heating describes the motion of a conductive fluid under the influence of an electric field, which generates heat due to electrical resistance. This phenomenon is observed in various applications, including microfluidics, electro-hydrodynamic systems, and industrial heating

processes [34]. The heating effect depends on factors like fluid properties, electric field strength, and flow conditions. Elboughdiri et al. [35] highlighted that the Joule heating significantly alters the temperature distribution, affecting fluid viscosity, density, and velocity profiles. In forced convection, the additional heat influences boundary layer development, enhancing or disrupting thermal equilibrium. In natural convection, Joule heating may introduce buoyancy-driven flow variations. Hasan et al. [36] deliberated the effects of entropy production and Joule heating for MHD fluid flow for a thermally non-homogeneous coolant system. In microfluidic applications, controlled Joule heating is used for precise temperature regulation, affecting chemical reactions, mixing efficiency, and biological assays. In industrial processes, like electrochemical systems and molten metal flows, it aids in maintaining optimal temperatures for processing. Ghaderi et al. [37] discovered that Joule heating affects thermal profiles by introducing non-uniform temperature gradients in the fluid. The heat generated increases the local temperature, leading to thermal stratification and possible hotspots. This alters heat conduction and convection mechanisms, modifying velocity fields and flow stability. Ullah et al. [38] studied Joule heating effects on time-based micro-polar fluid flow past a horizontal revolving sheet. Abdeljawad et al. [39] discussed this type of effect on fluid flow through Dacry-Forchheimer medium with Cattaneo-Christov flux model effects. In microfluidics, controlled heating enhances precision, while in larger systems, excessive heating can lead to overheating and efficiency losses. Variations in thermal profiles influence phase transitions, reaction rates, and energy dissipation. Tahiri et al. [40] scrutinized Joule heating effects on fluid flow through the micro-channel. Proper design and control of Joule heating are vital to optimizing performance while minimizing undesirable thermal effects in engineering and industrial applications.

A novel exploration of the Carreau ternary hybrid nanofluid past a bi-directional extending sheet incorporates the multiple physical effects that are not comprehensively examined together in other studies and is taken into consideration in this effort. The novelty factors of this research article are:

- Unlike conventional analyses that focus on nanofluids and hybrid nanofluids, we consider a ternary hybrid nanofluid flow composed of TiO_2, $CoFe_2O_4$, and MgO nanoparticles in a water-based fluid, offering enhanced rheological and thermal properties.
- This analysis includes the velocity slip conditions along both axes, significantly impacting the momentum transfer and is of paramount importance to novel understandings of the flow control mechanics.
- This analysis includes the influences of thermal-dependent and space-dependent heat sources, Joule heating, viscous dissipation, and thermal radiation, providing a more realistic model for heat transport in porous media.
- The governing equations are transformed into a dimensionless system and analyzed using the homotopy analysis method, which ensures enhanced accuracy and great convergence control compared to numerical and traditional perturbation techniques.

Our objectives of this article are:

- To develop a robust mathematical model for the Carreau ternary hybrid nanofluid past a bi-directional extending sheet using porous media, thermal convective, and slip conditions.
- To investigate the impacts of velocity slip, internal heat generation, magnetic field, and thermal radiation on the velocity and temperature distributions.
- To investigate the influences of thermal-dependent and space-dependent heat sources on heat transfer mechanisms.
- To investigate the influences of dimensionless factors (e.g., Biot number, Weissenberg number, stretching ratio factor, and Eckert number) on surface drag and heat transfer.

To validate the mathematical model by comparing our results with existing literature.

2. Formulation of the problem

Consider the three-dimensional Carreau ternary hybrid nanofluid flow over a bi-directional elongating sheet using porous media. TiO_2, $CoFe_2O_4$, and MgO nanoparticles are taken into consideration along with water as a base fluid to form a ternary hybrid nanofluid. The surface of the sheet is stretched with velocity $u_w(x)=cx$ along the x-direction and $v_w(y)=by$ along the y-direction such that c and b are fixed positive numbers. The magnetic field, having strength B_0, is applied to the flow system in the normal direction, as portrayed in Figure 1. The flow is influenced by the velocity slip and convective conditions. The flow is convectively heated by a hot working fluid with temperature T_f, such that $T_f > T_w$ where T_w is the surface temperature. Additionally, the impacts of thermal-dependent and space-dependent heat sources, thermal radiation, viscous dissipation, and Joule heating are taken into consideration. Thus, the major equations are [41–44]:

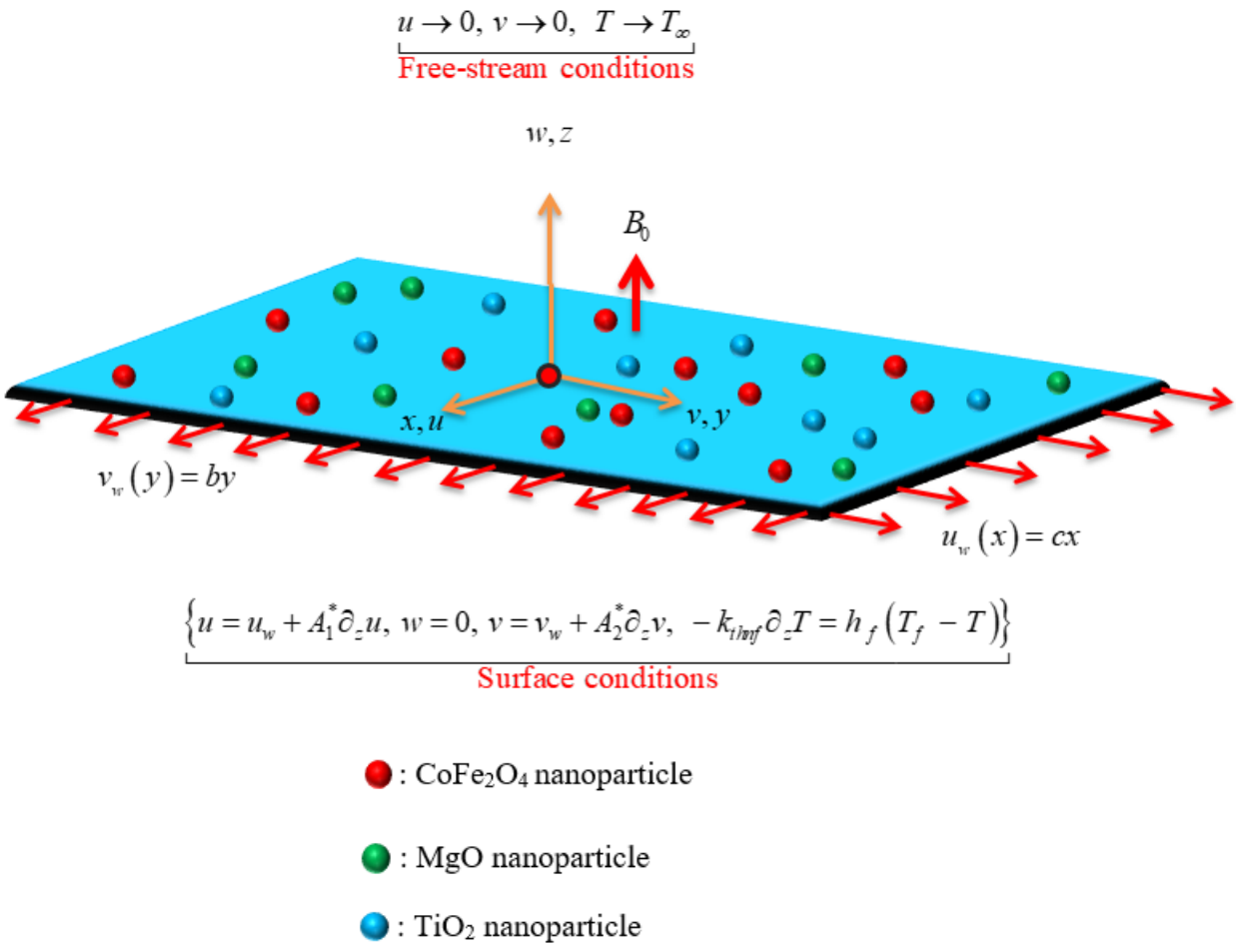

Figure 1. Flow geometry.

Continuity equation:

$$\partial_x u + \partial_y v + \partial_z w = 0. \tag{1}$$

Momentum equations:

$$\rho_{thnf}\left(u\partial_x u+v\partial_y u+w\partial_z u\right)=\mu_{thnf}\partial_{zz}u\begin{bmatrix}\left(1+\delta^2\left(\partial_z u\right)^2\right)^{\frac{n-1}{2}}+\\(n-1)\delta^2\left(\partial_z u\right)^2\left(1+\delta^2\left(\partial_z u\right)^2\right)^{\frac{n-3}{2}}\end{bmatrix}-\sigma_{thnf}B_0^2u-\frac{\mu_{thnf}}{K}u, \tag{2}$$

$$\rho_{thnf}\left(u\partial_x v+v\partial_y v+w\partial_z v\right)=\mu_{thnf}\partial_{zz}v\begin{bmatrix}\left(1+\delta^2\left(\partial_z v\right)^2\right)^{\frac{n-1}{2}}+\\(n-1)\delta^2\left(\partial_z v\right)^2\left(1+\delta^2\left(\partial_z v\right)^2\right)^{\frac{n-3}{2}}\end{bmatrix}-\sigma_{thnf}B_0^2v-\frac{\mu_{thnf}}{K}v. \tag{3}$$

Temperature equation:

$$\begin{aligned}\left(\rho C_p\right)_{thnf}\left(u\partial_x T+v\partial_y T+w\partial_z T\right)&=\left(k_{thnf}+\frac{16\sigma^* T_\infty^3}{3k^*}\right)\frac{\partial^2 T}{\partial z^2}+Q_T\left(T-T_\infty\right)\\&+Q_S\left(T_w-T_\infty\right)\exp\left(-a\zeta\right)+\sigma_{thnf}B_0^2\left(u^2+v^2\right)+\mu_{thnf}\left(\left(\partial_z u\right)^2+\left(\partial_z v\right)^2\right).\end{aligned} \tag{4}$$

The corresponding BCs are:

$$\begin{aligned}u=u_w+A_1^*\partial_z u, w=0, v=v_w+A_2^*\partial_z v, -k_{thnf}\partial_z T=h_f\left(T_f-T\right)\ at\ z=0,\\u\to, v\to 0,\ T\to T_\infty,\ \ as\ z\to\infty.\end{aligned} \tag{5}$$

The density is defined as defined as [45]:

$$\rho_{thnf}=\left(1-\mathrm{X}_1\right)\left\{\left(1-\mathrm{X}_2\right)\left[\left(1-\mathrm{X}_3\right)+\mathrm{X}_3\frac{\rho_3}{\rho_f}\right]+\mathrm{X}_2\frac{\rho_2}{\rho_f}\right\}+\mathrm{X}_1\frac{\rho_1}{\rho_f}. \tag{6}$$

The specific heat is defined as [45]:

$$\left(\rho C_p\right)_{thnf}=\left(1-\mathrm{X}_1\right)\left\{\left[\left(1-\mathrm{X}_3\right)+\mathrm{X}_3\frac{\left(\rho C_p\right)_3}{\left(\rho C_p\right)_f}\right]\left(1-\mathrm{X}_2\right)+\mathrm{X}_2\frac{\left(\rho C_p\right)_2}{\left(\rho C_p\right)_f}\right\}+\mathrm{X}_1\frac{\left(\rho C_p\right)_1}{\left(\rho C_p\right)_f}. \tag{7}$$

The dynamic viscosity is defined as [45]:

$$\mu_{thnf}=\frac{\mu_f}{\left(1-\mathrm{X}_1\right)^{2.5}\left(1-\mathrm{X}_2\right)^{2.5}\left(1-\mathrm{X}_3\right)^{2.5}}. \tag{8}$$

The thermal conductivity is defined [45]:

$$\begin{aligned}\frac{k_{thnf}}{k_{hnf}}&=\frac{k_1+2k_{hnf}-2\mathrm{X}_1\left(k_{hnf}-k_1\right)}{k_1+2k_{hnf}+\mathrm{X}_1\left(k_{hnf}-k_1\right)},\\\frac{k_{hnf}}{k_{nf}}&=\frac{k_2+2k_{nf}-2\mathrm{X}_1\left(k_{nf}-k_2\right)}{k_2+2k_{nf}+\mathrm{X}_2\left(k_{nf}-K_2\right)},\\\frac{k_{nf}}{k_f}&=\frac{k_3+2k_f-2\mathrm{X}_3\left(k_f-k_3\right)}{k_3+2k_f+\mathrm{X}_3\left(k_f-k_3\right)}.\end{aligned} \tag{9}$$

The electrical conductivity for ternary hybrid nanofluid is defined as [45]:

$$\begin{aligned}\frac{\sigma_{thnf}}{\sigma_{hnf}} &= \frac{(1+2\mathrm{X}_1)\sigma_1-(1-2\mathrm{X}_1)\sigma_{hnf}}{(1-\mathrm{X}_1)\sigma_1+(1+\mathrm{X}_1)\sigma_{hnf}},\\ \frac{\sigma_{hnf}}{\sigma_{nf}} &= \frac{(1+2\mathrm{X}_2)\sigma_2+(1-2\mathrm{X}_2)\sigma_{nf}}{(1-\mathrm{X}_2)\sigma_2+(1+\mathrm{X}_2)\sigma_{nf}},\\ \frac{\sigma_{NF}}{\sigma_F} &= \frac{(1+2\mathrm{X}_3)\sigma_3+(1-2\mathrm{X}_3)\sigma_f}{(1-\mathrm{X}_3)\sigma_3+(1+\mathrm{X}_3)\sigma_f}.\end{aligned} \tag{10}$$

The experimental values of the considered nanoparticles and water are defined in Table 1 [46–48].

Table 1. Experimental values of base fluid and nanoparticles.

Properties	H_2O	TiO_2	$CoFe_2O_4$	MgO
$\rho\left[\mathrm{kg.m^{-3}}\right]$	997.1	4250	4907	3560
$C_p\left[\mathrm{J.kg.K^{-1}}\right]$	4179	686.2	700	955
$k\left[\mathrm{W.m^{-1}.K^{-1}}\right]$	0.613	8.9538	3.7	45
$\sigma\left[\mathrm{S.m^{-1}}\right]$	0.05	2.38×10^{6}	5.51×10^{9}	1.42×10^{-3}

The similarity transformations are described as [49–51]:

$$\zeta = z\sqrt{\frac{c}{\nu_f}},\quad u = F'(\zeta)xc, \Im v = cyG'(\zeta)\quad \theta(\zeta)=\frac{T-T_\infty}{T_f-T_\infty},\quad w=-\sqrt{c\nu_f}\left(G(\zeta)+F(\zeta)\right). \tag{11}$$

Employing Eq (11) in Eqs (1)–(5) we have:

$$\begin{aligned}&\frac{\Re_1}{\Re_2}\left\{\left(1+We^2F''^2(\zeta)\right)^{\frac{n-3}{2}}\left(1+nWe^2F''^2(\zeta)\right)\right\}F'''(\zeta)-\\ &\left\{F'^2(\zeta)-\left(G(\zeta)+F(\zeta)\right)F''(\zeta)\right\}-\frac{\Re_3}{\Re_2}MF'(\zeta)-\frac{\Re_1}{\Re_2}\lambda F'(\zeta)=0,\end{aligned} \tag{12}$$

$$\begin{aligned}&\frac{\Re_1}{\Re_2}\left\{\left(1+We^2G''^2(\zeta)\right)^{\frac{n-3}{2}}\left(1+nWe^2G''^2(\zeta)\right)\right\}G'''(\zeta)-\\ &\left\{G'^2(\zeta)-\left(G(\zeta)+F(\zeta)\right)G''(\zeta)\right\}-\frac{\Re_3}{\Re_2}MG'(\zeta)-\frac{\Re_1}{\Re_2}\lambda G'(\zeta)=0,\end{aligned} \tag{13}$$

$$\begin{aligned}&\frac{1}{\mathrm{Pr}}\left(\frac{\Re_4}{\Re_5}+\frac{Rd}{\Re_5}\right)\theta''(\zeta)+\left\{F(\zeta)+G(\zeta)\right\}\theta'(\zeta)+\frac{Q_{Td}}{\Re_5}\theta(\zeta)+\frac{Q_{Sd}}{\Re_5}\exp(-a\zeta)\\ &+\frac{\Re_3}{\Re_5}M\left(Ec_xF'(\zeta)+Ec_yG'(\zeta)\right)+\frac{\Re_1}{\Re_5}\left(Ec_xF''(\zeta)+Ec_yG''(\zeta)\right)=0.\end{aligned} \tag{14}$$

With corresponding BCs:

$$\begin{aligned} &F(0)=0, F'(0)=1+A_1F''(0),\ F'(\infty)\to 0,\\ &G(0)=0,\ G'(0)=\alpha+A_2G''(0),\ G'(\infty)\to 0,\\ &\Re_4\theta'(0)=-Bi_T\left(\theta(0)-1\right),\ \theta(\infty)\to 0. \end{aligned} \tag{15}$$

Here, $\Re_1=\frac{\mu_{thnf}}{\mu_f}, \Re_2=\frac{\rho_{thnf}}{\rho_f}, \Re_3=\frac{\sigma_{thnf}}{\sigma_f}, \Re_4=\frac{k_{thnf}}{k_f}$ and $\Re_5=\frac{\left(\rho C_p\right)_{thnf}}{\left(\rho C_p\right)_f}$ are the thermophysical relations, $\Pr=\frac{\left(\mu_f C_p\right)_f}{k_f}$ designates the Prandtl number, $Rd=\frac{16\sigma^\star T_\infty^3}{3k^\star k_f}$ shows the thermal radiation parameter, $Q_{Sd}=\frac{Q_S}{c\left(\rho C_p\right)_f}$ shows the space-dependent heat source, $Bi_T=\frac{h_f}{k_f}\sqrt{\frac{\nu_f}{c}}$ defines the Biot number, $Q_{Td}=\frac{Q_T}{c\left(\rho C_p\right)_f}$ shows the thermal-dependent heat source, $Ec_x=\frac{u_w^2}{\left(C_p\right)_f\left(T_f-T_\infty\right)}$ shows the Eckert number along the primary direction, $Ec_y=\frac{v_w^2}{\left(C_p\right)_f\left(T_f-T_\infty\right)}$ shows the Eckert number along the secondary direction, $We=\delta u_w\sqrt{\frac{c}{\nu_f}}$ shows the local Weissenberg number, $\lambda=\frac{\mu_f}{c\rho_f K}$ shows the porosity factor, $\alpha=\frac{b}{c}$ expresses the stretching ratio factor, $M=\frac{\sigma_f B_0^2}{c\rho_f}$ designates the magnetic factor, $A_1=A_1^*\sqrt{\frac{c}{\nu_f}}$ is the slip factor for primary velocity, and $A_2=A_2^*\sqrt{\frac{c}{\nu_f}}$ is the slip factor for secondary velocity.

3. Physical quantities

The physical quantities for the current work are described as follows:
The skin frictions along the primary and secondary are respectively defined as:

$$C_{fx}=\frac{2\tau_{wx}}{\rho u_w^2},\ C_{fy}=\frac{2\tau_{wy}}{\rho u_w^2}, \tag{16}$$

where τ_{wx} and τ_{wy}, the shear stresses along *x*- and *y*-directions, are defined as:

$$\tau_{wx}=\left[\mu_{thnf}\partial_z u\left(1+\delta^2\left(\partial_z u\right)^2\right)\right]^{\frac{n-1}{2}}\Bigg|_{z=0},\ \tau_{wy}=\left[\mu_{thnf}\partial_z v\left(1+\delta^2\left(\partial_z v\right)^2\right)\right]^{\frac{n-1}{2}}_{z=0}\Bigg|. \tag{17}$$

The Nusselt number is defined as:

$$Nu_x = \frac{xq_w}{k_f\left(T_f - T_\infty\right)}, \tag{18}$$

where q_w, the heat flux is defined as:

$$q_w = -\left(k_{thnf} + \frac{16T^3\sigma^*}{3k^*}\right)\partial_z T\Big|_{z=0}. \tag{19}$$

Using Eq (11), Eq (16) is reduced as:

$$\begin{aligned} C_{fx}Re_x^{1/2} &= \frac{2}{\Re_1}\left(1+We^2F''^2\left(0\right)\right)F''\left(0\right), \\ C_{fy}Re_y^{1/2} &= \frac{2}{\Re_1}\left(1+We^2G''^2\left(0\right)\right)G''\left(0\right). \end{aligned} \tag{20}$$

Using Eq (11), Eq (18) is reduced as:

$$Nu_xRe_x^{-1/2} = -\left(\Re_4 + Rd\right)\theta'\left(0\right). \tag{21}$$

4. Solution method

To evaluate the solution of Eqs (12)−(14) with Eq (15), we use the homotopy analysis method (HAM). It is used to determine the solution to nonlinear ODEs. By introducing an auxiliary parameter ($\hbar$), HAM enables the flexibility to adjust and ensure convergence. This feature makes it highly effective in solving a wide range of nonlinear problems. This approach requires an initial guess, which is described for the current problem in the following lines:

$$F_0\left(\zeta\right) = \frac{1}{\left(1+A_1\right)}\left(1-e^{-\zeta}\right),\ G_0\left(\zeta\right) = \frac{\alpha}{\left(1+A_2\right)}\left(1-e^{-\zeta}\right),\ \theta\left(\zeta\right) = \frac{Bi_T}{\Re_4\left(1+Bi_T\right)}\left(e^{-\zeta}\right). \tag{22}$$

The linear operators are chosen as:

$$F_0\left(\zeta\right) = F'''\left(\zeta\right) - F'\left(\zeta\right),\ G_0\left(\zeta\right) = G'''\left(\zeta\right) - G'\left(\zeta\right),\ \theta_0\left(\zeta\right) = \theta''\left(\zeta\right) - \theta\left(\zeta\right). \tag{23}$$

With properties:

$$\begin{aligned} L_F\left(\pi_1 + e^{-\zeta}\pi_2 + e^{\zeta}\pi_3\right) &= 0, \\ L_G\left(\pi_4 + e^{-\zeta}\pi_5 + e^{\zeta}\pi_6\right) &= 0, \\ L_\theta\left(e^{-\zeta}\pi_7 + e^{\zeta}\pi_8\right) &= 0, \end{aligned} \tag{24}$$

where $\pi_1 - \pi_8$ are the constants.

5. HAM convergence

HAM ensures convergence through the convergence control parameter ($\hbar$), which enables flexible adjustment of the solution series. Factor ($\hbar$) plays a vital role in defining and monitoring the area of convergence for series solutions. For this problem, $\hbar$-curves are sketched in Figure 2(a)−(c)

to secure the convergence for each profile of the solution series on specific domains. The convergence of velocity distribution along the x-axis ensures the domain $-1.0 \le \hbar_f \le 0.2$. The convergence of velocity distribution along the y-axis ensures the domain $-2.0 \le \hbar_g \le 0.00$. The convergence of thermal profiles ensures the domain $-2.3 \le \hbar_\theta \le 0.7$.

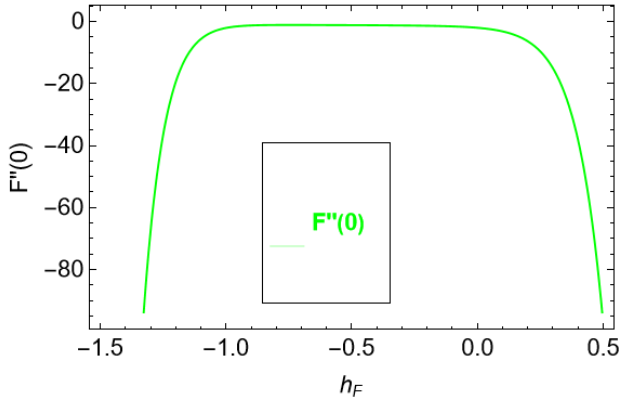

(a) $\hbar-$curve for $F''(0)$

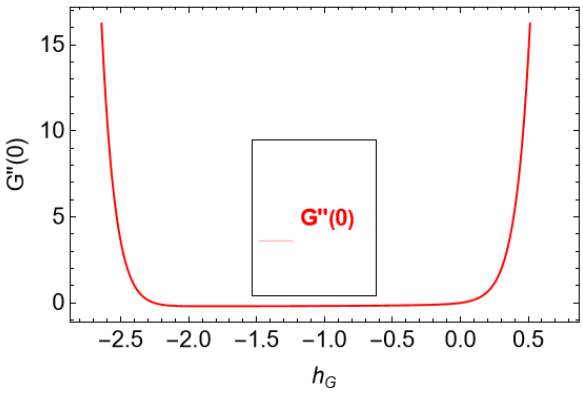

(b) $\hbar-$curve for $G''(0)$

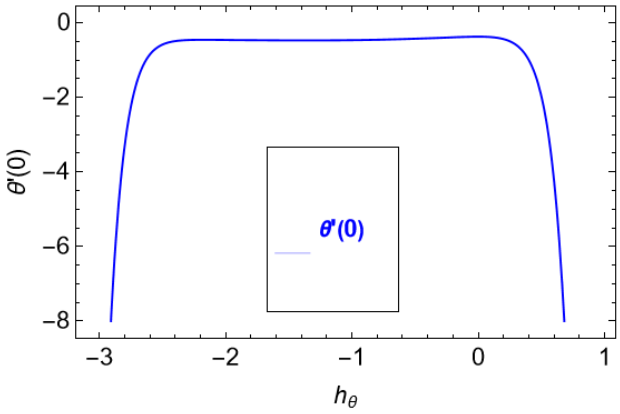

(c) $\hbar-$curve for $\theta'(0)$.

Figure 2. $\hbar-$curves for $F''(0), G''(0)$ and $\theta'(0)$.

6. Validation

To ensure the validation of current results, we compare our results with established studies of Yusuf et al. [52], Mabood and Das [53], and Xu and Lee [54]. This comparison is illustrated for various values of ($C_{fx}Re_x^{1/2}$, $C_{fy}Re_y^{1/2}$) in Tables 2 and 3 regarding variations in α and M and fixing other factors. Table 2 confirms the validation of the method for variations in α, while Table 3 confirms the validation method for variations in M.

Table 2. Comparison of our results with Yusuf et al. [52].

α		0.0	0.2	0.4	0.6	0.8	1.0
Ref. [52]	$C_{fx}Re_x^{1/2}$	1.0	1.039495	1.075788	1.109944	1.142489	1.173721
	$C_{fy}Re_y^{1/2}$	0.0	0.148737	0.349209	0.590529	0.866683	1.173721
Present	$C_{fx}Re_x^{1/2}$	1.0	1.039495	1.075788	1.109944	1.142489	1.173721
	$C_{fy}Re_y^{1/2}$	0.0	0.148737	0.349209	0.590529	0.866683	1.173721

Table 3. Comparison of our results with Mabood and Das [53] and Xu and Lee [54].

	M	0.0	1.0	5.0	10.0	50.0	100.0	500.0	1000.0
$C_{fx}Re_x^{1/2}$	Yusuf et al. [52]	1.000008	1.414214	2.44949	3.316625	7.141428	10.04988	22.38303	31.63858
	Mabood and Das [53]	1.000008	1.414214	2.44949	3.316625	7.141428	10.04988	22.38303	31.63858
	Xu and Lee [54]	-	1.41421	2.4494	3.3166	7.1414	10.0498	22.38302	-
	Present	1.000008	1.414214	2.44949	3.316625	7.141428	10.04987	22.38302	31.63858

7. Discussion of results

We examine ternary hybrid Carreau nanofluid flow on a porous bi-directional elongating sheet. The nanoparticles of TiO_2, $CoFe_2O_4$, and MgO mix with water to get a ternary hybrid nanofluid. The flow is influenced by slip conditions of velocities along the x- and y-axes. The impacts of thermal- and space-dependent heat sources, thermal radiation, viscous dissipation, and Joule heating are used in this study. Moreover, magnetic effects are used along the z-axis, which is normal to the flow direction. The major equations are solved through the HAM in dimensionless form. The impacts of various emerging factors on velocities and temperature are discussed in the upcoming paragraphs. The default values of the embedded factors are chosen as, $Rd = 0.1$, $Q_{Sd} = 0.1$, $Bi_T = 0.5$, $Q_{Td} = 0.1$, $Ec_x = 0.1$, $Ec_y = 0.1$, $We = 0.5$, $\lambda = 0.2$, $\alpha = 0.5$, $M = 1.0$, $A_1 = 0.5$, and $A_2 = 0.5$.

The effects of the velocity slip factor A_1 along the x-axis on primary velocity distribution $\{F'(\zeta)\}$ are portrayed in Figure 3, in which $\{F'(\zeta)\}$ has a declining behavior for $A_1 = 0.1, 0.2, 0.3, 0.4$. As the velocity slip factor increases along the x-axis, the interaction between the fluid and the surface weakens, leading to a reduction in momentum transfer from the surface to the fluid. This causes lower shear forces and less energy being conveyed to the fluid, causing a decrease in $\{F'(\zeta)\}$. Physically, this can be interpreted as a greater resistance to acceleration due to reduced adherence of fluid particles to the surface, which inhibits the development of a strong velocity profile

$\{F'(\zeta)\}$. Consequently, the overall motion of the fluid slows down, leading to a reduction in primary velocity $\{F'(\zeta)\}$. The effects of velocity slip factor A_2 along the y-axis on $\{G'(\zeta)\}$ are portrayed in Figure 4, in which $\{G'(\zeta)\}$ has a declining behavior for $A_2 = 0.5, 0.6, 0.7, 0.8$. As the velocity slip factor A_2 increases along the y-axis, the interaction between the fluid and the surface weakens, reducing the transfer of momentum from the primary flow to the secondary flow. This results in a decrease in secondary velocity $\{G'(\zeta)\}$, which is typically driven by shear forces and boundary layer effects. Physically, this can be understood as a reduction in the strength of secondary flow structures, such as vortices, due to lower frictional forces at the boundary. Consequently, the flow becomes more aligned with the primary direction, and the intensity of secondary motion $\{G'(\zeta)\}$ diminishes, as illustrated in Figure 4.

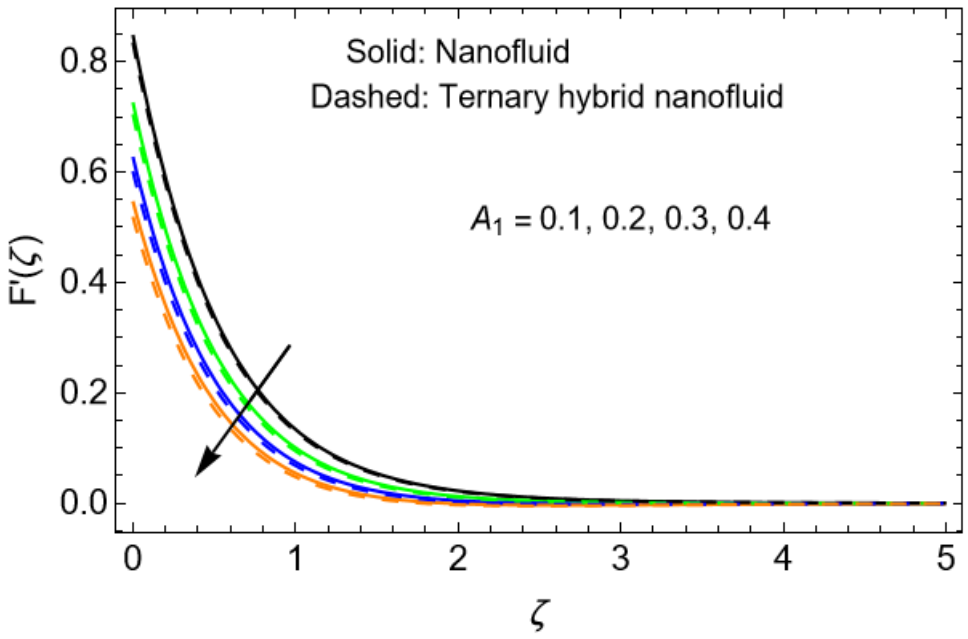

Figure 3. Effect of A_1 on $F'(\zeta)$.

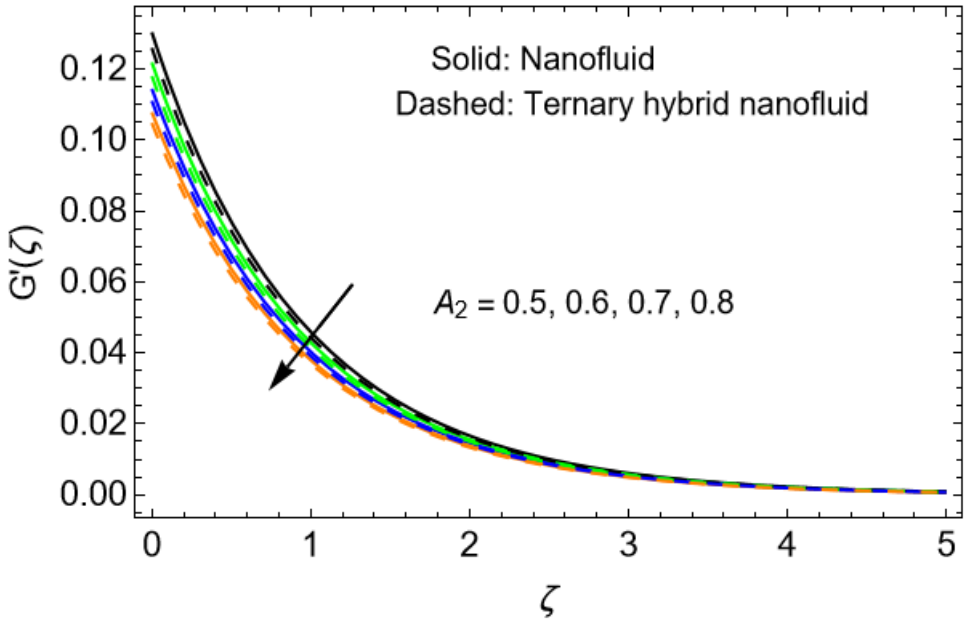

Figure 4. Effect of A_2 on $G'(\zeta)$.

The effects of the magnetic factor M on $\{F'(\zeta)\}$ are portrayed in Figure 5, in which $\{F'(\zeta)\}$ has a declining behavior for $M = 0.5, 1.0, 1.5, 2.0$. As M **(**magnetic factor**)** increases the Lorentz force-generated and acts as a resistive force, opposing the fluid motion. This results in a reduction of $\{F'(\zeta)\}$. In the case of ternary hybrid nanofluid flow, which consists of multiple nanoparticles (TiO_2, $CoFe_2O_4$ and MgO), the combined effects of enhanced viscosity and intensified electromagnetic interactions further amplify this resistive effect, leading to a more noticeable velocity reduction than a single-component nanofluid. The increased particle-particle and particle-fluid interactions in ternary hybrid nanofluids contribute to greater momentum diffusion, thereby reinforcing the deceleration effect under a magnetic field. The effects of the magnetic factor M on $\{G'(\zeta)\}$ are portrayed in Figure 6, in which $\{G'(\zeta)\}$ has a declining behavior for $M = 0.5, 1.0, 1.5, 2.0$. The reduction in secondary velocity $\{G'(\zeta)\}$ with increasing magnetic factor is due to the Lorentz force, which acts as a resistive force against the fluid motion. In the case of ternary hybrid nanofluid flow, the presence of multiple nanoparticles enhances the electrical conductance of the fluid, leading to a stronger interaction with the applied magnetic field. This causes a more significant damping effect on the secondary velocity $\{G'(\zeta)\}$ compared to a regular nanofluid. The increased resistance slows down the transverse motion, making the suppression of secondary flow more noticeable in ternary hybrid nanofluids.

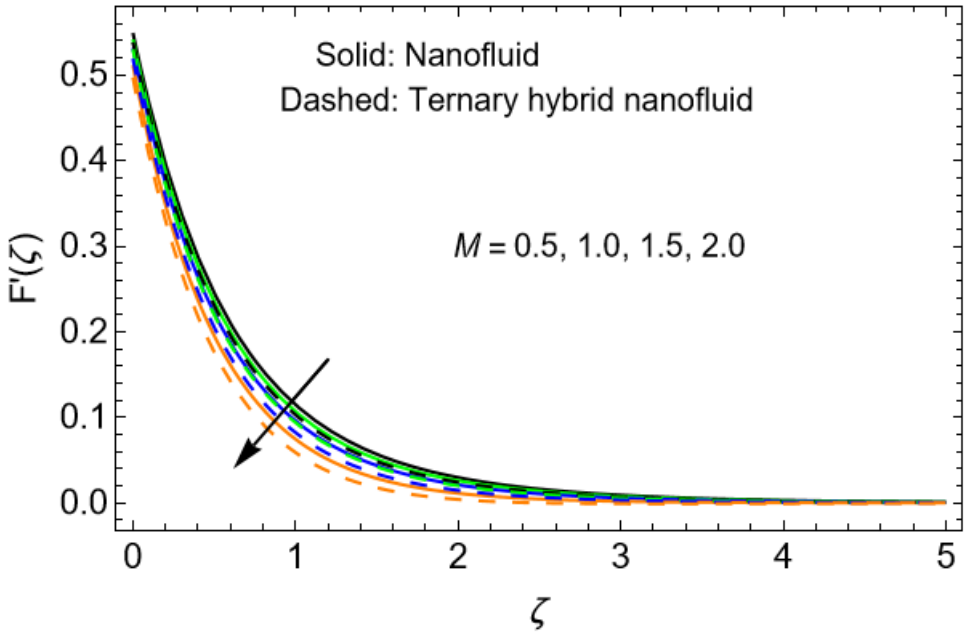

Figure 5. Effect of M on $F'(\zeta)$.

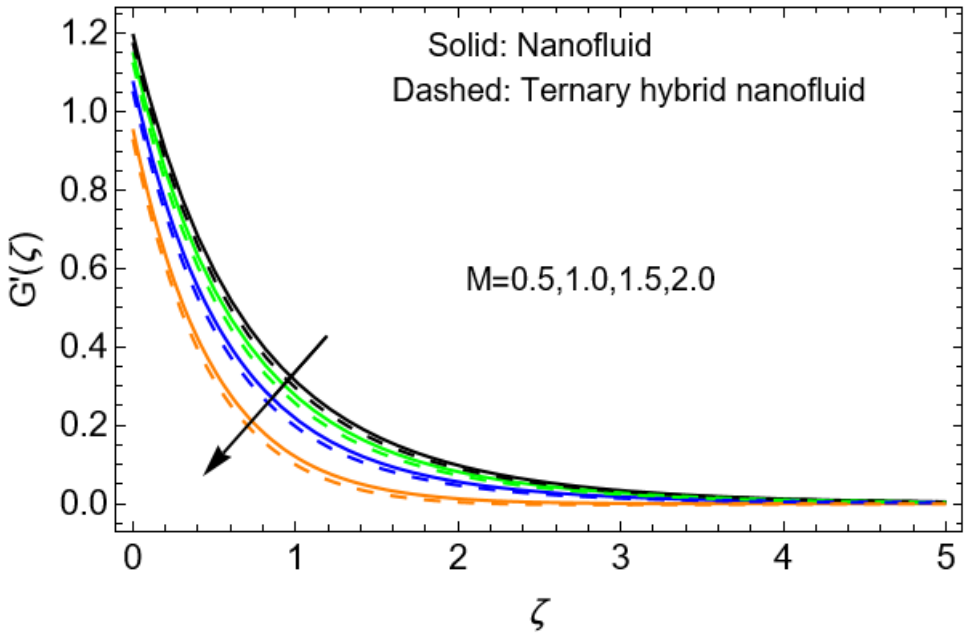

Figure 6. Effect of M on $G'(\zeta)$.

The effects of stretching ratio factor $\{\alpha\}$ on $\{F'(\zeta)\}$ are portrayed in Figure 7, in which $\{F'(\zeta)\}$ has a declining behavior for $\alpha = 0.5, 1.0, 1.5, 2.0$. As stretching ratio factor $\{\alpha\}$ increases, the fluid experiences greater elongation, leading to a decrease in primary velocity $\{F'(\zeta)\}$. Physically, this occurs because as the sheet's surface stretches, the fluid's particles spread over a larger area, causing a redistribution of momentum. This stretching effect reduces the forward motion of the fluid's particles, as more energy is used in the elongation process rather than maintaining the initial velocity. In fluid dynamics, this is observed when an increasing stretching ratio leads to a thinner boundary layer,

which reduces the fluid's ability to sustain its primary velocity due to increased resistance and strain effects. The effects of stretching ratio factor $\{\alpha\}$ on $\{G'(\zeta)\}$ are portrayed in Figure 8, in which $\{G'(\zeta)\}$ has an augmenting behavior for $\alpha = 0.5, 0.6, 0.7, 0.8$. As the stretching ratio factor $\{\alpha\}$ increases, the fluid elements experience greater elongation, leading to enhanced momentum transfer. This results in an increase in secondary velocity $\{G'(\zeta)\}$, which represents the motion perpendicular to the primary flow direction. Physically, this can be interpreted as the stretching force inducing stronger transverse flow effects due to increased shear stress and strain rates within the fluid. In practical scenarios, like in polymer processing or boundary layer flows, a higher stretching ratio can enhance mixing and influence the overall stability of the flow field.

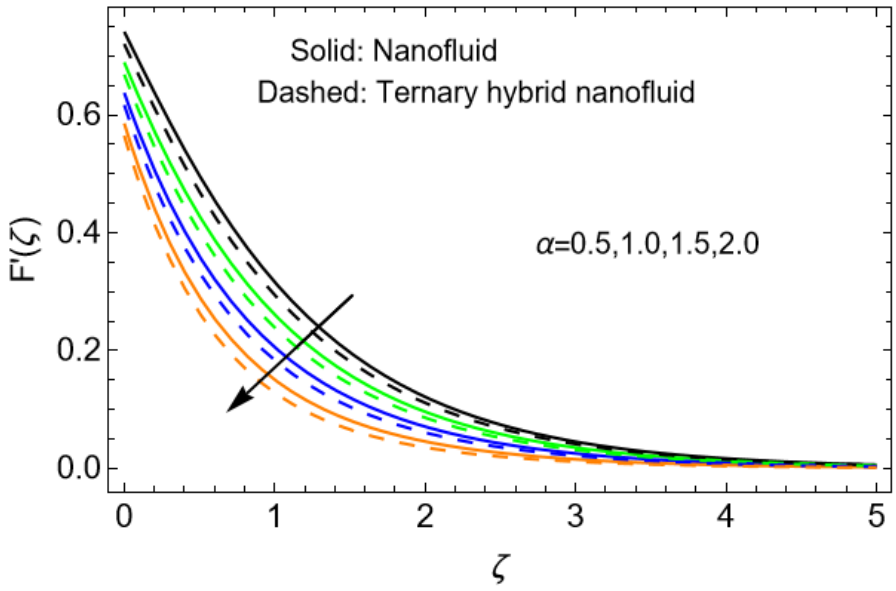

Figure 7. Effect of α on $F'(\zeta)$.

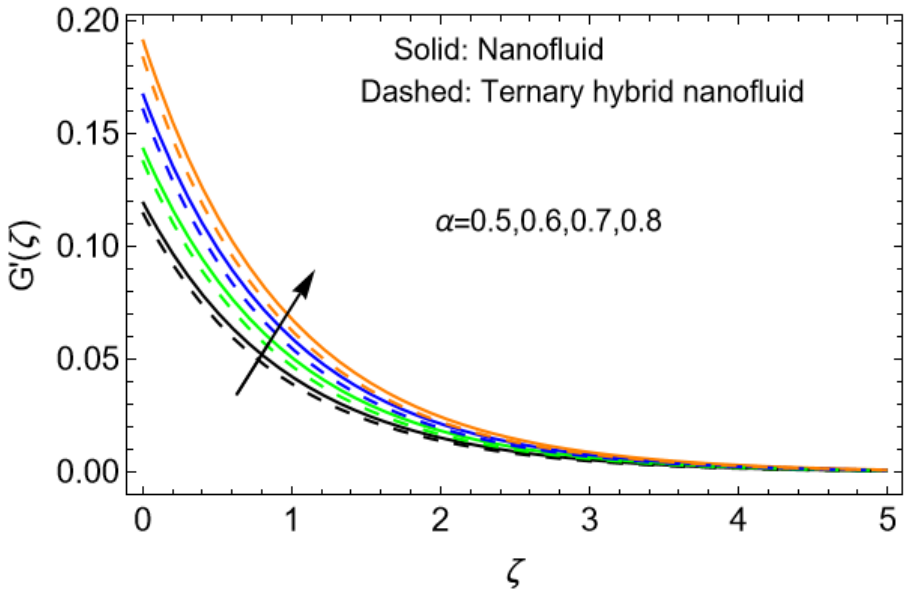

Figure 8. Effect of α on $G'(\zeta)$.

The effects of porosity factor $\{\lambda\}$ on $\{F'(\zeta)\}$ are portrayed in Figure 9, in which $\{F'(\zeta)\}$ has a declining behavior for $\lambda = 0.1, 0.2, 0.3, 0.4$. As porosity increases $\{\lambda\}$, $\{F'(\zeta)\}$ decreases because a more porous medium offers greater resistance to flow. Higher porosity means more void spaces within the material, leading to increased interactions between the fluid and the solid matrix on the sheet's surface. These interactions cause energy dissipation through friction and turbulence, reducing the overall velocity of the fluid. Additionally, a highly porous medium leads to fluid dispersion, further slowing down the primary flow direction. This effect is commonly observed in porous rock formations, filtration systems, and other fluid transport processes in porous materials. The effects of porosity factor $\{\lambda\}$ on $\{G'(\zeta)\}$ are portrayed in Figure 10, in which $\{G'(\zeta)\}$ has a declining behavior for $\lambda = 0.1, 0.2, 0.3, 0.4$. As the porosity increases, more void spaces are present in the medium, reducing the resistance to fluid flow. This leads to a decrease in the shear forces that drive secondary velocity components, which are typically caused by variations in pressure and velocity gradients within the fluid. In porous media on the surface of the sheet, the increased porosity enables the fluid to pass more freely through the voids, reducing the need for significant transverse or secondary motion $\{G'(\zeta)\}$. Consequently, the secondary velocity diminishes, and the overall momentum exchange in the transverse direction weakens.

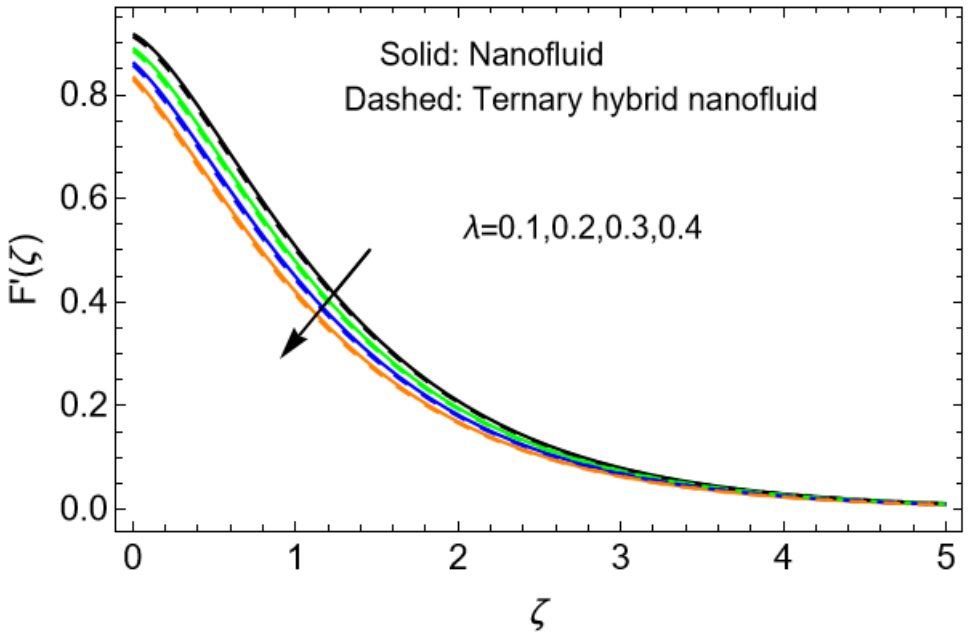

Figure 9. Effect of λ on $F'(\zeta)$.

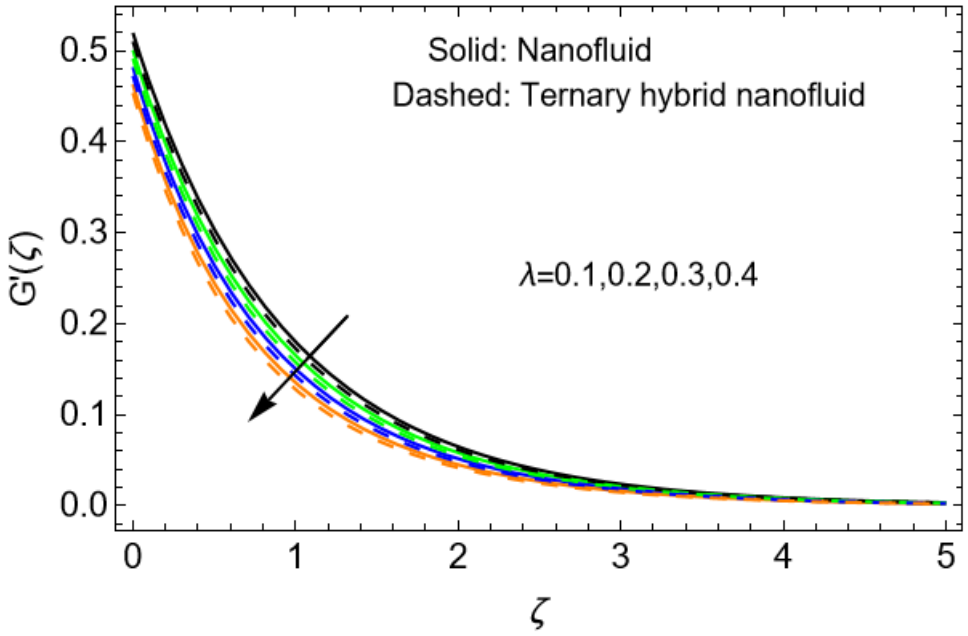

Figure 10. Effect of λ on $G'(\zeta)$.

The effects of the local Weissenberg number $\{We\}$ on $\{F'(\zeta)\}$ are portrayed in Figure 11, in which $\{We\}$ has a declining behavior for $We = 0.1, 0.2, 0.3, 0.4$. As the local Weissenberg number $\{We\}$ increases, the fluid's elasticity becomes more dominant. This causes increased resistance to deformation and inhibits the fluid's ability to flow smoothly. Consequently, $\{F'(\zeta)\}$ decreases because the fluid stores more elastic energy instead of converting it into motion. This effect is particularly significant in viscoelastic fluids, where higher $\{We\}$ values cause strain strengthening, reducing the overall momentum transfer and slowing the flow in the primary direction $\{F'(\zeta)\}$. The effects of the local Weissenberg number $\{We\}$ on $\{G'(\zeta)\}$ are portrayed in Figure 12, in which $\{We\}$ has a declining behavior for $We = 0.1, 0.2, 0.3, 0.4$. As $\{We\}$ surges, the fluid's elasticity becomes more dominant, leading to stronger normal stress differences. This elasticity resists secondary flows $\{G'(\zeta)\}$, which are typically induced by shear or other forces perpendicular to the primary flow direction. Consequently, the secondary velocity $\{G'(\zeta)\}$ decreases because the fluid's internal structure resists deformation and redistributes stress in a way that suppresses transverse motion. This effect is particularly significant in flows where viscoelasticity is crucial, such as in polymeric or biological fluids.

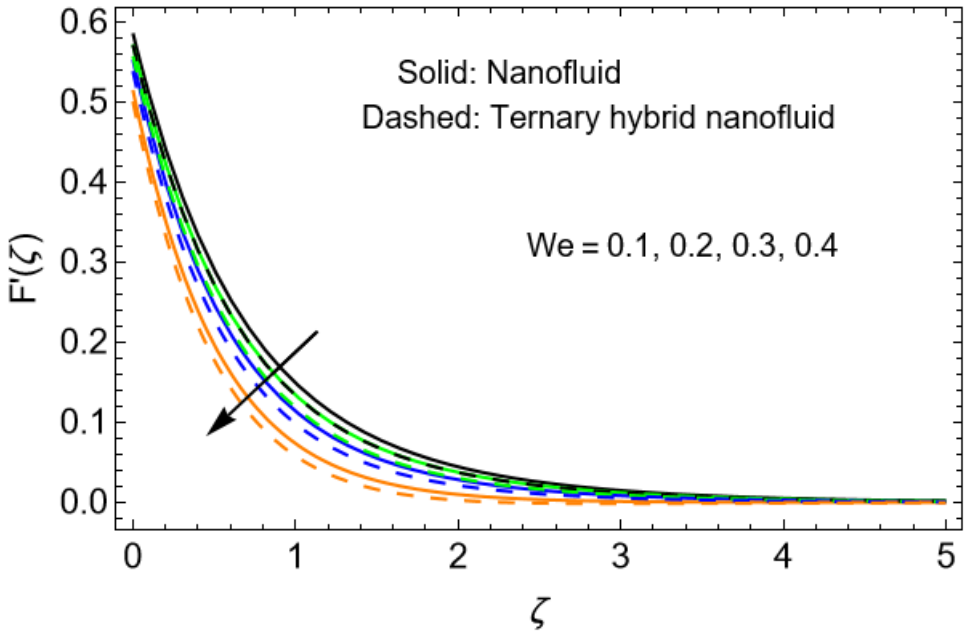

Figure 11. Effect of We on $F'(\zeta)$.

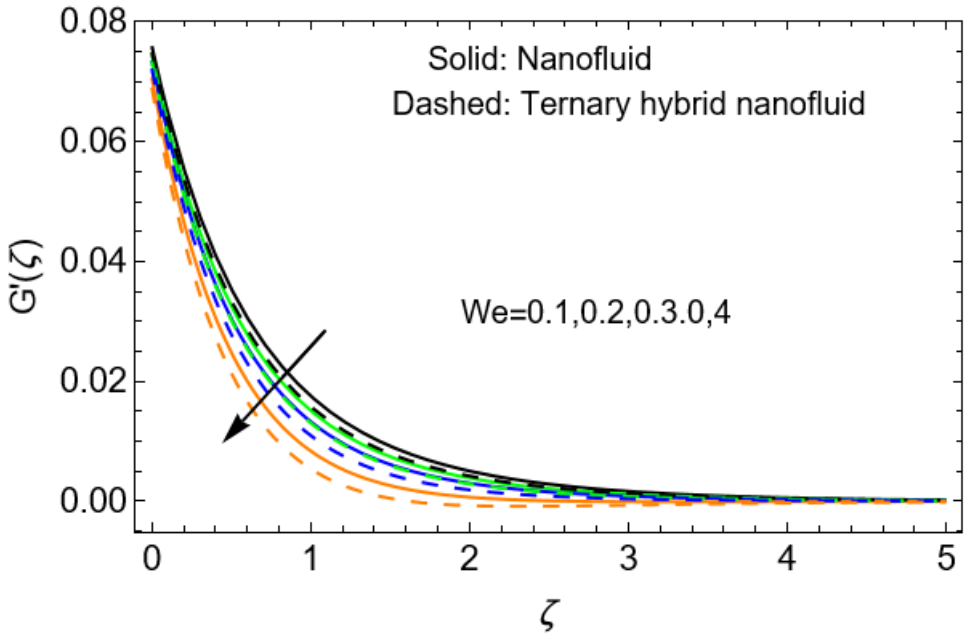

Figure 12. Effect of We on $G'(\zeta)$.

The effects of thermal Biot number $\{Bi_T\}$ on the thermal distribution $\{\theta(\zeta)\}$ are portrayed in Figure 13, in which $\{Bi_T\}$ has an augmenting behavior for $Bi_T = 0.1, 0.2, 0.3, 0.4$. As $\{Bi_T\}$ increases, it indicates that heat conduction inside the fluid becomes relatively slower compared to heat transfer across the surface. Physically, this means that the temperature gradients within the fluid become more noticeable, leading to non-uniform thermal distribution $\{\theta(\zeta)\}$. In practical terms, when $\{Bi_T\}$ is low (less than 0.1), the fluid tends to have a nearly uniform temperature since internal

conduction is much faster than surface convection. However, as $\{Bi_T\}$ grows, heat takes longer to diffuse internally, causing significant temperature variations inside the fluid. Moreover, this impact is more significant in the case of ternary hybrid nanofluid in comparison to nanofluid.

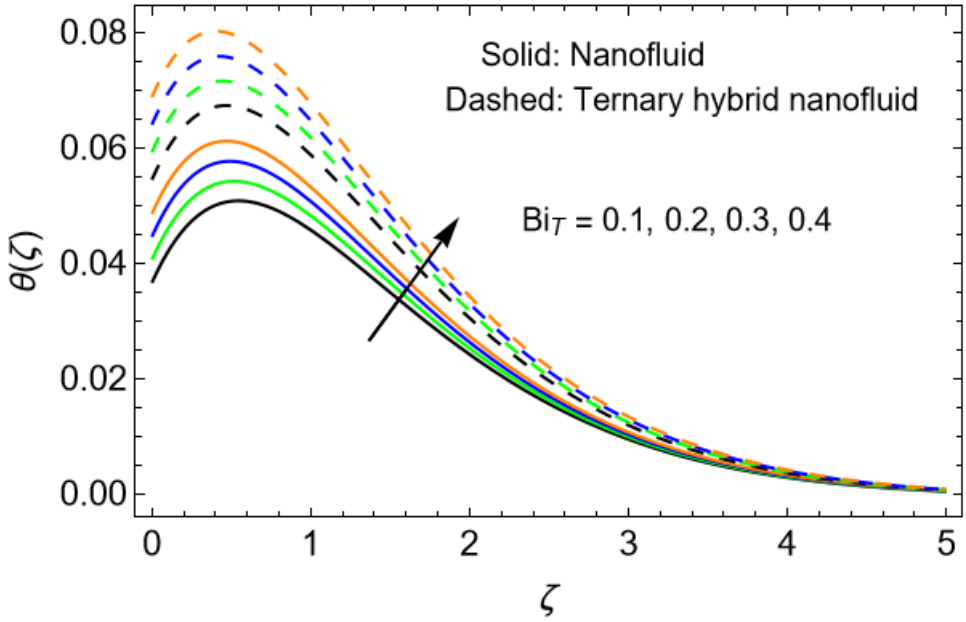

Figure 13. Effect of Bi_T on $\theta(\zeta)$.

The effects of the thermal-dependent heat source $\{Q_{Td}\}$ on the thermal distribution $\{\theta(\zeta)\}$ are portrayed in Figure 14, in which $\{Q_{Td}\}$ has an augmenting behavior for $Q_{Td} = 0.1, 0.2, 0.3, 0.4$. As the heat source $\{Q_{Td}\}$ increases, more thermal energy is introduced into the system, causing a rise in temperature. This results in enhanced thermal distribution $\{\theta(\zeta)\}$ due to increased conduction, convection, and radiation. The heat spreads more efficiently through the medium, affecting temperature gradients and fluid flow characteristics, especially in heat transfer applications. The augmentation in $\{\theta(\zeta)\}$ is more noticeable in ternary hybrid nanofluid flow than nanofluid flow due to improved thermal conductivity and heat absorption properties. The synergistic effect of multiple nanoparticles enhances energy transport, reducing temperature differences and improving heat dissipation efficiency in engineering and industrial applications.

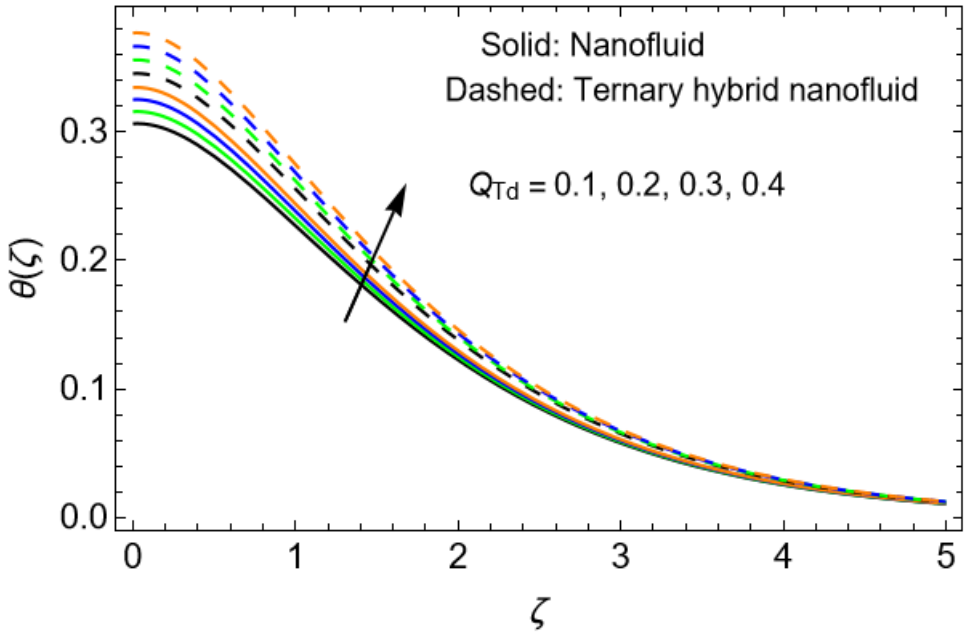

Figure 14. Effect of Q_{Td} on $\theta(\zeta)$.

The effects of space-dependent heat source $\{Q_{Sd}\}$ on the thermal distribution $\{\theta(\zeta)\}$ are portrayed in Figure 15, in which $\{Q_{Sd}\}$ has an augmenting behavior for $Q_{Sd} = 0.1, 0.2, 0.3, 0.4$. As the space-dependent heat source $\{Q_{Sd}\}$ increases, the thermal energy distribution within the system becomes non-uniform, leading to spatial variations in temperature. This results in enhanced thermal distribution $\{\theta(\zeta)\}$, where regions closer to the heat source experience higher temperatures, while conduction and convection help spread heat throughout the medium. The intensity and pattern of thermal augmentation depend on the heat source's spatial variation, the thermal conductivity of the medium, and the flow characteristics of the fluid. In fluid-based heat transfer systems, this spatially varying heat input significantly affects the thermal boundary layer, leading to complex temperature gradients and influencing energy transport efficiency. The enhancement in thermal profiles $\{\theta(\zeta)\}$ is more noticeable in ternary hybrid nanofluid flow than in nanofluid flow due to the superior thermal conductivity and synergistic effects of multiple nanoparticles. This combination improves heat absorption, enhances convection, and leads to more efficient energy transport, resulting in greater thermal augmentation than conventional nanofluids.

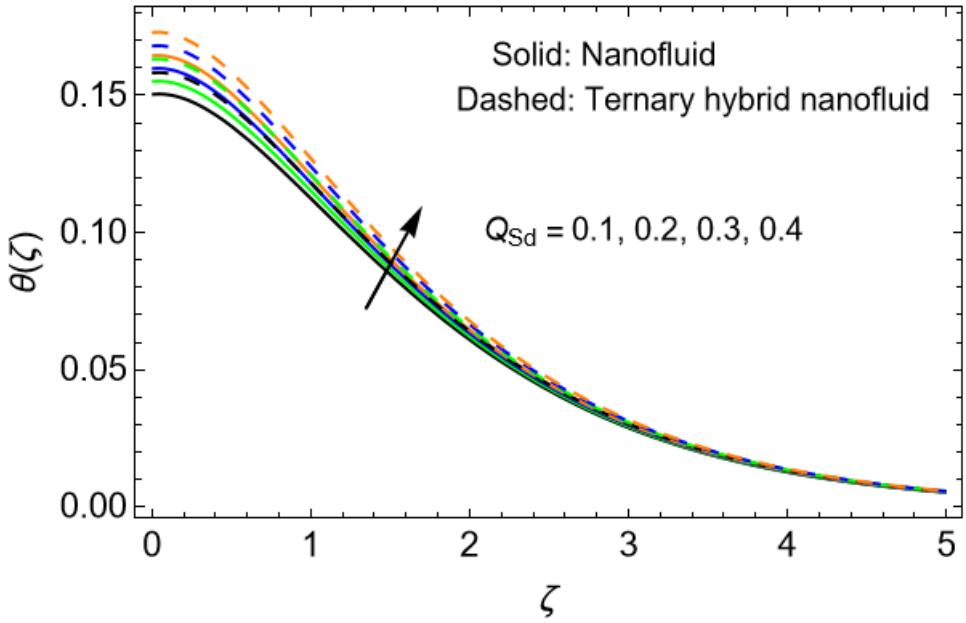

Figure 15. Effect of Q_{Sd} on $\theta(\zeta)$.

The effects of the radiation factor $\{Rd\}$ on the thermal distribution $\{\theta(\zeta)\}$ are portrayed in Figure 16, in which $\{Rd\}$ has an augmenting behavior for $Rd = 0.1,\ 0.2,\ 0.3,\ 0.4$. When the thermal radiation factor $\{Rd\}$ increases, it enhances energy transfer through radiation, leading to a higher thermal distribution $\{\theta(\zeta)\}$ in the fluid. This occurs because radiation contributes additional heat energy, intensifying the thermal gradients and raising the overall temperature. In fluid dynamics, this effect is more noticeable in thermally conductive materials, where increased radiation absorption accelerates the energy exchange. In nanofluid and hybrid nanofluid flows, the presence of nanoparticles further enhances thermal conductivity, amplifying this effect. The augmentation is particularly significant in ternary hybrid nanofluids, as they contain multiple nanoparticles that synergistically improve heat transfer, leading to superior thermal performance compared to conventional nanofluids.

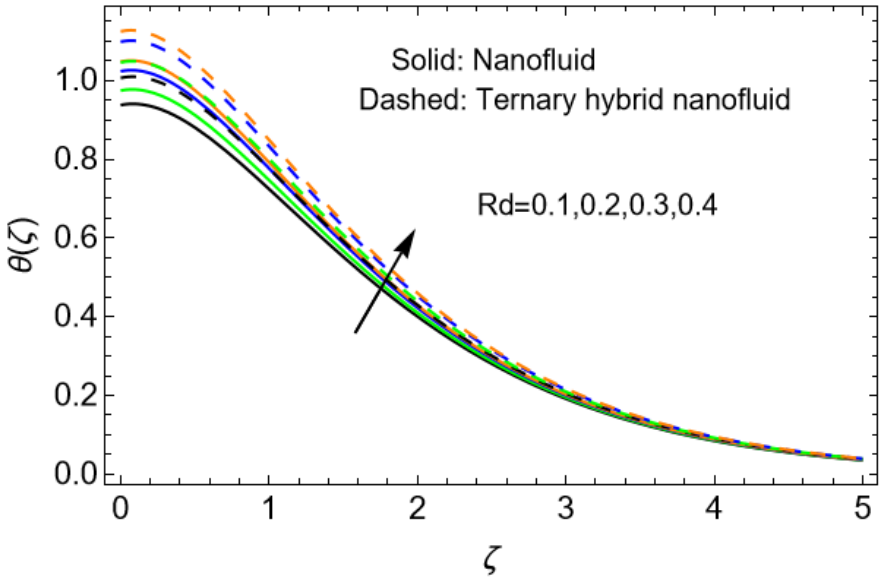

Figure 16. Effect of Rd on $\theta(\zeta)$.

The effects of Eckert number $\{Ec_x\}$ along the primary direction on the thermal distribution $\{\theta(\zeta)\}$ are portrayed in Figure 17, in which $\{Ec_x\}$ has an augmenting behavior for $Ec_x = 0.1, 0.2, 0.3, 0.4$. As $\{Ec_x\}$ increases along the primary direction, more mechanical energy is converted into heat due to viscous dissipation, leading to enhanced thermal distribution $\{\theta(\zeta)\}$. This effect is particularly important in high-speed and high-viscous flows, where frictional heating significantly influences the temperature field. In nanofluid flow, suspended nanoparticles improve thermal conductance, but in ternary hybrid nanofluids, the synergistic interaction of three different nanoparticles enhances heat transfer even further. Combining multiple nanoparticles provides superior thermal performance and greater surface area for heat exchange.

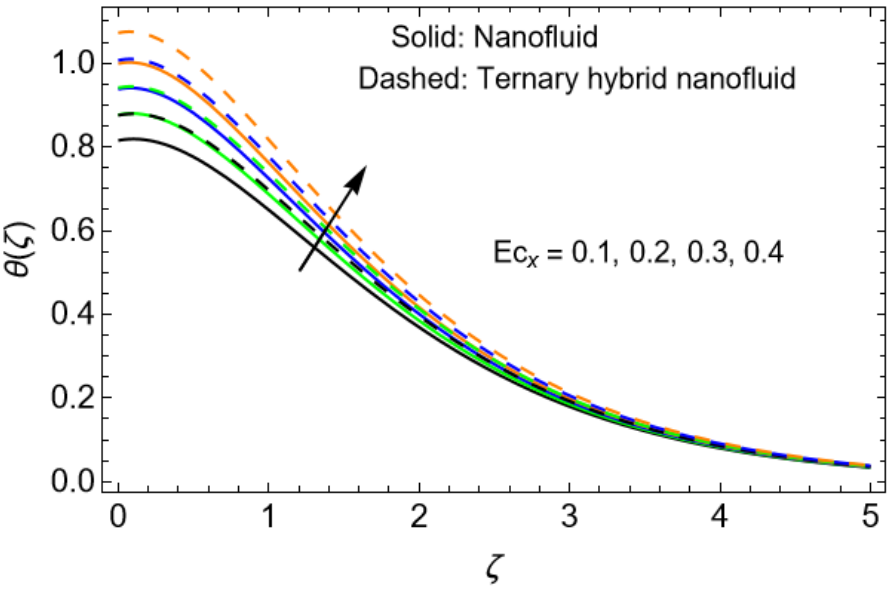

Figure 17. Effect of Ec_x on $\theta(\zeta)$.

The effects of Eckert number $\{Ec_y\}$ along the primary direction on the thermal distribution $\{\theta(\zeta)\}$ are portrayed in Figure 18, in which $\{Ec_y\}$ has an augmenting behavior for $Ec_y = 0.1, 0.2, 0.3, 0.4$. An increase in the Eckert number $\{Ec_y\}$ along the secondary direction implies that more mechanical energy is being converted to thermal energy due to viscous effects. This results in an augmentation of the thermal distribution $\{\theta(\zeta)\}$, meaning that the fluid temperature rises as more heat is generated through internal friction. In boundary layer flows, higher $\{Ec_y\}$ values enhance the temperature near the surface of the sheet, leading to greater heat accumulation and altering the overall thermal gradient in the system. This effect is particularly noticeable in high-speed and high-viscosity flows, where viscous heating plays a dominant role in energy transfer.

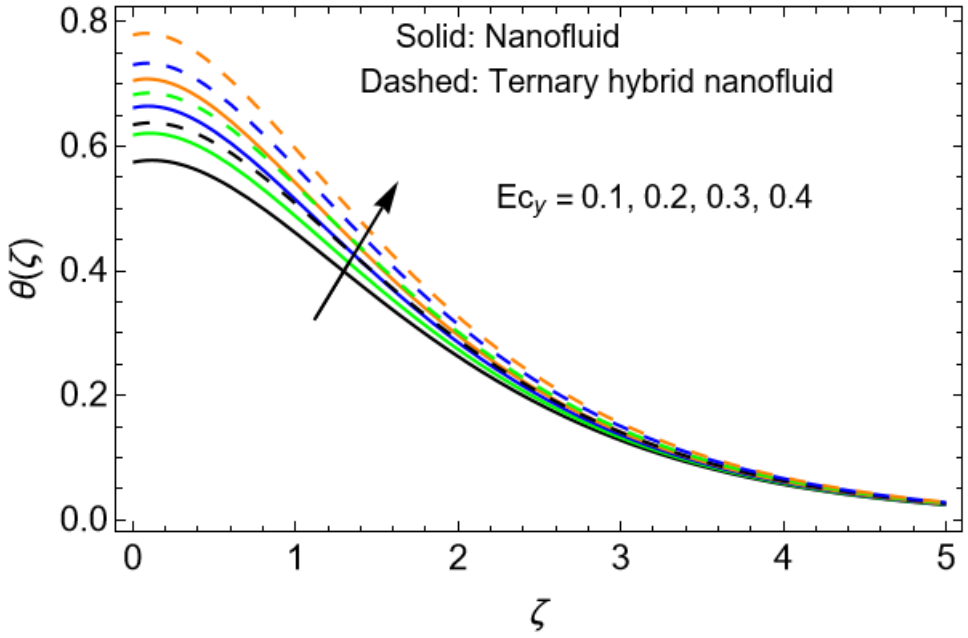

Figure 18. Effect of Ec_y on $\theta(\zeta)$.

The effects of $\{M\}$ on $\{\theta(\zeta)\}$ are portrayed in Figure 19, in which $\{M\}$ has an augmenting behavior for $M = 0.1, 0.2, 0.3, 0.4$. As the magnetic factor $\{M\}$ increases, charged particles within the fluid flow system experience greater Lorentz forces, altering their motion and influencing heat transfer mechanisms. In conductive materials (fluids), stronger magnetic fields can induce swirl currents, leading to Joule heating, which raises the thermal energy of the system. In fluids, magnetic effects modify convection patterns, redistributing heat and potentially enhancing the thermal gradients. Additionally, for fluid flow on the bi-directionally elongating sheet, changes in magnetization can further affect fluid temperature by altering thermal conductance. The augmentation in thermal distribution with increasing magnetic factor arises from these combined effects on the flow system.

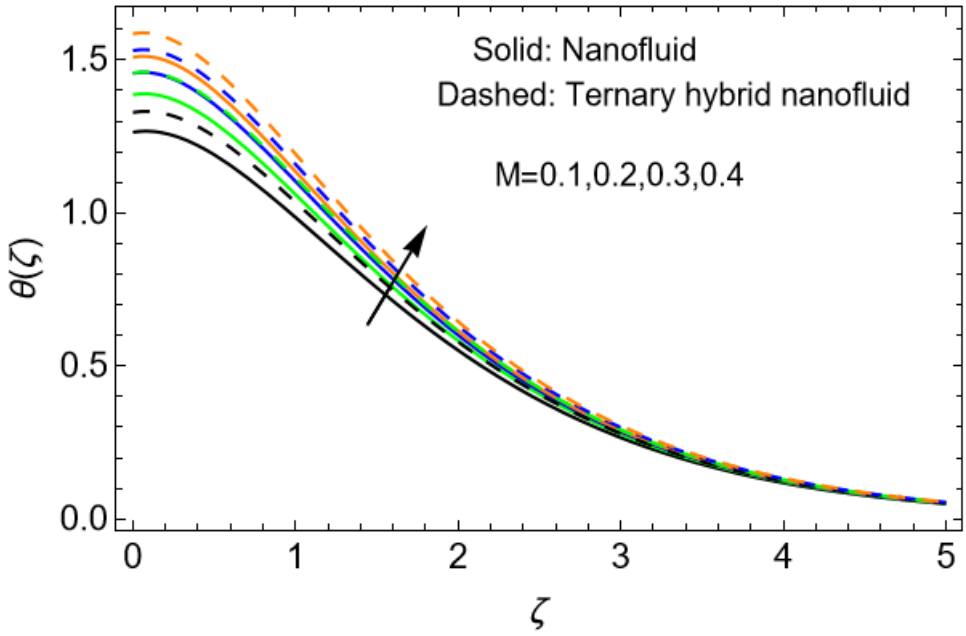

Figure 19. Effect of M on $\theta(\zeta)$.

Table 1 demonstrates the experimental values of base fluid and nanoparticles. Table 2 illustrates the comparison of current results with Yusuf et al. [52], while Table 3 provides the comparison of current results with Mabood & Das [53] and Xu & Lee [54]. Table 4 portrays the impacts of various factors on $C_{fx}Re_x^{1/2}$ and $C_{fy}Re_y^{1/2}$. Here, it is revealed that as the magnetic factor M, porosity factor λ, and velocity slip factors A_1 and A_2 increase along the x- and y-axes, there is a corresponding rise in skin frictions $C_{fx}Re_x^{1/2}$, and $C_{fy}Re_y^{1/2}$. The magnetic field influences the fluid flow by introducing a resistive force, which alters the velocity profile and enhances shear stress at the surface. Similarly, the porosity factor affects the permeability of the medium, modifying the interaction between the fluid and the boundary, leading to changes in frictional forces. The velocity slip factors also contribute to the variation in shear stress by reducing the no-slip condition's effectiveness. Consequently, the combined effects of these parameters result in an overall augmentation of skin friction in both the primary and secondary directions, i.e., $C_{fx}Re_x^{1/2}$ and $C_{fy}Re_y^{1/2}$. Table 5 contains the impacts of various factors on Nusselt number $Nu_xRe_x^{-1/2}$. Here, it has been revealed that as the radiation factor Rd increases, it enhances the overall thermal energy transfer, leading to an increase in the Nusselt number $Nu_xRe_x^{-1/2}$, which signifies improved convective heat transfer. Similarly, the space-dependent heat source factor Q_{Sd} contributes to localized variations in heat generation, intensifying thermal gradients, thereby augmenting the Nusselt number $Nu_xRe_x^{-1/2}$. The thermal-dependent heat source factor Q_{Td} further influences heat transfer by altering the rate of heat production based on temperature variations, which enhances convective efficiency. Additionally, a rise in the Eckert numbers Ec_x and Ec_y, which represents the relative significance of kinetic energy to enthalpy, leads to higher heat dissipation due to viscous dissipation effects, further boosting the Nusselt number $Nu_xRe_x^{-1/2}$.

Table 4. Effects of M, λ, A_1 and A_2 on $C_{fx}Re_x^{1/2}$ and $C_{fy}Re_y^{1/2}$.

M	λ	A_1	A_2	$C_{fx}Re_x^{1/2}$	$C_{fy}Re_y^{1/2}$
0.5				1.455653	0.576436
0.6				1.504345	0.597543
0.7				1.553567	0.616532
	0.1			1.253356	0.224442
	0.2			1.268643	0.232463
	0.3			1.279654	0.254325
		0.1		1.424675	0.224565
		0.2		1.433566	0.256754
		0.3		1.444335	0.286586
			0.1	1.597643	0.597643
			0.2	1.622567	0.605426
			0.3	1.654367	0.613465

Table 5. Effects of Rd, Q_{Sd}, Q_{Td}, Ec_x and Ec_y on $Nu_xRe_x^{-1/2}$.

Rd	Q_{Sd}	Q_{Td}	Ec_x	Ec_y	$Nu_xRe_x^{-1/2}$
0.1					1.543455
0.2					1.554356
0.3					1.568642
	0.1				1.296544
	0.2				1.327884
	0.3				1.359875
		0.1			1.486536
		0.2			1.503256
		0.3			1.527542
			0.1		1.633677
			0.2		1.705363
			0.3		1.779976
				0.1	1.668098
				0.2	1.764348
				0.3	1.868965

8. Conclusions

In this work, we examine ternary hybrid Carreau nanofluid flow on a porous bi-directional elongating sheet. The nanoparticles of TiO_2, $CoFe_2O_4$, and MgO mix with water to get a ternary hybrid nanofluid. The flow is influenced by slip conditions of velocities along the x- and y-axes. The impacts of thermal- and space-dependent heat sources, thermal radiation, viscous dissipation, and Joule heating are used in this study. Moreover, magnetic effects are used along the z-axis, which is normal to the flow direction. The major equations are solved through the HAM in dimensionless form. After an in-depth investigation of the work, it is noticed that:

- With progression in velocity slip factors along x- and y-axes and magnetic factor, there is a reduction in both velocities.
- An upsurge in the stretching ratio factor results in lessening primary flow and intensification in secondary flow.
- Growth in porosity factor and local Weissenberg number causes a lessening in both velocities.
- Thermal distribution augments with a surge in thermal Biot number, magnetic factor, space-dependent heat source parameter, radiation factor, and Eckert numbers along primary and secondary directions.
- The skin friction coefficients increase with growth in magnetic factor, porosity factor, and velocity slip factors along the x- and y-axes.
- The Nusselt number escalates with a surge in radiation factor, space-dependent heat source factor, thermal-dependent heat source factor, and Eckert numbers along x- and y-axes.
- Our results of this work are validated through comparative analysis by matching our data with established results. A fine promise has been noticed among all the results.

Limitations: This analysis is limited to time-independent flow assumptions, which do not capture transient effects that may occur in real-world applications. A ternary hybrid nanofluid contains TiO_2, $CoFe_2O_4$, and MgO nanoparticles with water as a base fluid. However, the incorporation of other metals, metal oxides, nonmetal and polymeric nanoparticles with other base fluids like ethylene glycol, oil, etc. could exhibit different thermal and flow characteristics.

Future research: In the future, the present research can be extended to explore the time-dependent flow conditions to better understand the transient effect in practical applications. Extending this research to analyze the impacts of different base fluids and nanoparticle composition could provide broader insights into the nanofluid behavior. In addition, the investigation of alternative non-Newtonian models, such as Cross, Casson, or Maxwell models, could enhance the applicability of the analysis to various biomedical and industrial processes.

Author contributions

Humaira Yasmin and Anwar Saeed have modelled the problem in mathematical form; Rawan Bossly and Fuad S. Alduais have solved the problem; Fuad S. Alduais, Humaira Yasmin and Afrah Al-Bossly have prepared all the graphs; Anwar Saeed, Fuad S. Alduais and Afrah Al-Bossly have written the original manuscript. All authors have read and approved the final version of the manuscript for publication.

Use of Generative-AI tools declaration

The authors declare they have not used Artificial Intelligence (AI) tools in the creation of this article.

Funding statement

This work was supported by the Deanship of Scientific Research, the Vice Presidency for Graduate Studies and Scientific Research, King Faisal University, Saudi Arabia (Grant No. KFU251554). This study is supported via funding from Prince Sattam bin Abdulaziz University project number (PSAU/2024/R/1446).

Conflict of interest

The authors declare no competing interests.

References

1. S. U. S. Choi, J. A. Eastman, *Enhancing thermal conductivity of fluids with nanoparticles*, Argonne National Lab.(ANL), Argonne, IL (United States), 1995.
2. A. Ali, Z. Khan, M. Sun, T. Muhammad, K. A. M. Alharbi, Numerical investigation of heat and mass transfer in micropolar nanofluid flows over an inclined surface with stochastic numerical approach, *Eur. Phys. J. Plus*, **139** (2024), 1–25. https://doi.org/10.1140/epjp/s13360-024-05676-0
3. A. M. Galal, F. M. Alharbi, M. Arshad, M. M. Alam, T. Abdeljawad, Q. M. Al-Mdallal, Numerical investigation of heat and mass transfer in three-dimensional MHD nanoliquid flow with inclined magnetization, *Sci. Rep.*, **14** (2024), 1207. https://doi.org/10.1038/s41598-024-51195-4
4. E. A. Algehyne, F. M. Alamrani, A. Khan, K. A. Khan, S. A. Lone, A. Saeed, A comparative analysis of the blood-based hybrid nanofluid flow containing Cu and CuO nanoparticles over an exponentially extending surface, *Proc. I. Mech. Eng. E-J. Proc.*, 2024. https://doi.org/10.1177/09544089241235063
5. V. P. Kalbande, M. S. Choudhari, Y. N. Nandanwar, Hybrid nano-fluid for solar collector based thermal energy storage and heat transmission systems: A review, *J. Energy Storage*, **86** (2024), 111243. https://doi.org/10.1016/j.est.2024.111243
6. A. Kazemian, A. Salari, T. Ma, H. Lu, Application of hybrid nanofluids in a novel combined photovoltaic/thermal and solar collector system, *Sol. Energy*, **239** (2022), 102–116. https://doi.org/10.1016/j.solener.2022.04.016
7. K. Guedri, A. Khan, N. Sene, Z. Raizah, A. Saeed, A. M. Galal, Thermal flow for radiative ternary hybrid nanofluid over nonlinear stretching sheet subject to Darcy-Forchheimer phenomenon, *Math. Probl. Eng.*, **2022** (2022). https://doi.org/10.1155/2022/3429439
8. Y. Mehmood, A. Alsinai, M. Bilal, S. Iqbal, A. U. K. Niazi, N. Faisal, Numerical investigation of entropy generation on micropolar trihybrid nanofluid flow with blood as base fluid in a channel, *J. Math.*, **2024** (2024), 9583109. https://doi.org/10.1155/2024/9583109
9. S. Z. H. Shah, A. Ayub, S. Bhatti, U. Khan, A. Ishak, E. M. Sherif, et al., Aspects of inclined magnetohydrodynamics and heat transfer in a non-Newtonian tri-hybrid bio-nanofluid flow past a wedge-shaped artery utilizing artificial neural network scheme, *ZAMM-J. Appl. Math. Mech. Für Angew. Math. Und Mech.*, **104** (2024), e202400278. https://doi.org/10.1002/zamm.202400278
10. M. I. I. Rabby, M. W. Uddin, N. M. S. Hassan, M. Al Nur, R. Uddin, S. Istiaque, et al., Recent progresses in tri-hybrid nanofluids: A comprehensive review on preparation, stability, thermo-hydraulic properties, and applications, *J. Mol. Liq.*, 2024, 125257. https://doi.org/10.1016/j.molliq.2024.125257
11. M. D. Afifi, B. Jalili, A. Mirzaei, P. Jalili, D. Ganji, The effects of thermal radiation, thermal conductivity, and variable viscosity on ferrofluid in porous medium under magnetic field, *World J. Eng.*, **22** (2025), 218–231. http://org.doi/10.1108/WJE-09-2023-0402
12. S. Anwar, U. Ahmad, T. Sun, M. Ashraf, G. Rasool, Impact of solar radiation in the presence of temperature-dependent thermal conductivity of non-Newtonian Casson flow on natural convection heat transfer in plume generated due to the combined effects of heat source and aligned magnetic field, *Numer. Heat Transf. Part A Appl.*, 2024, 1–18. https://doi.org/10.1080/10407782.2024.2367089

13. G. Sarfraz, S. U. Khan, D. L. C. Ching, I. Khan, A. Mir, Y. Khan, et al., Influence of solar thermal radiations and convective boundary on $Al2O_3/H_2O$ transient model efficiency, *J. Radiat. Res. Appl. Sci.*, **17** (2024), 101117. https://doi.org/10.1016/j.jrras.2024.101117
14. M. Nayfeh, A. Nayfeh, A. Rezk, E. Bahceci, W. Alnaser, On silicon nanobubbles in space for scattering and interception of solar radiation to ease high-temperature induced climate change, *AIP Adv.*, **14** (2024). https://doi.org/10.1063/5.0187880
15. S. Nasir, A. Berrouk, Z. Khan, Efficiency assessment of thermal radiation utilizing flow of advanced nanocomposites on riga plate, *Appl. Therm. Eng.*, **242** (2024), 122531. https://doi.org/10.1016/j.applthermaleng.2024.122531
16. M. Sohail, K. Abodayeh, U. Nazir, Implementation of finite element scheme to study thermal and mass transportation in water-based nanofluid model under quadratic thermal radiation in a disk, *Mech. Time-Depend. Mater.*, **28** (2024), 1049–1072. https://doi.org/10.1007/s11043-024-09736-x
17. U. Farooq, A. Jan, M. Hussain, Impact of thermal radiations, heat generation/absorption and porosity on MHD nanofluid flow towards an inclined stretching surface: Non-similar analysis, *ZAMM-J. Appl. Math. Mech. Für Angew. Math. Und Mech.*, **104** (2024), e202300306. https://doi.org/10.1002/zamm.202300306
18. S. Bilal, M. B. Riaz, Thermofluidic transport of Williamson flow in stratified medium with radiative energy and heat source aspects by machine learning paradigm, *Int. J. Thermofluids*, **24** (2024), 100818. https://doi.org/10.1016/j.ijft.2024.100818
19. B. Ali, S. Jubair, M. I. H. Siddiqui, Numerical simulation of 3D Darcy-Forchheimer hybrid nanofluid flow with heat source/sink and partial slip effect across a spinning disc, *J. Porous Media*, **27** (2024). https://doi.org/10.1615/JPorMedia.2024051759
20. P. Jalili, S. M. S. Mousavi, B. Jalili, P. Pasha, D. D. Ganji, Thermal evaluation of MHD Jeffrey fluid flow in the presence of a heat source and chemical reaction, *Int. J. Mod. Phys. B*, **38** (2024), 2450113. https://doi.org/10.1142/S0217979224501133
21. K. Alqawasmi, K. A. M. Alharbi, U. Farooq, S. Noreen, M. Imran, A. Akgül, et al., Numerical approach toward ternary hybrid nanofluid flow with nonlinear heat source-sink and fourier heat flux model passing through a disk, *Int. J. Thermofluids*, **18** (2023), 100367. https://doi.org/10.1016/j.ijft.2023.100367
22. J. K. Madhukesh, I. E. Sarris, V. K, B. C. Prasannakumara, A. Abdulrahman, Computational analysis of ternary nanofluid flow in a microchannel with nonuniform heat source/sink and waste discharge concentration, *Numer. Heat Tr. A-Appl.*, 2023, 1–18. https://doi.org/10.1080/10407782.2023.2240509
23. G. Shankar, P. Deepalakshmi, E. P. Siva, D. Tripathi, O. A. Bég, Thermomagnetic peristaltic Casson flow in a microchannel containing a Darcy–Brinkman porous medium under the influence of oscillatory, thermal radiation, slip and heat source effects, *Pramana*, **99** (2025), 32. https://doi.org/10.1007/s12043-024-02869-1
24. M. V. Reddy, K. Vajravelu, P. Lakshminarayana, G. Sucharitha, Heat source and Joule heating effects on convective MHD stagnation point flow of Casson nanofluid through a porous medium with chemical reaction, *Numer. Heat Tr. B-Fund.*, **85** (2024), 286–304. https://doi.org/10.1080/10407790.2023.2233694
25. M. Abbas, N. Khan, M. S. Hashmi, R. K. Alhefthi, S. Rezapour, M. Inc, Thermal Marangoni convection in two-phase quadratic convective flow of dusty MHD trihybrid nanofluid with non-linear heat source, *Case Stud. Therm. Eng.*, **57** (2024), 104190. https://doi.org/10.1016/j.csite.2024.104190

26. K. Swain, S. M. Ibrahim, G. Dharmaiah, S. Noeiaghdam, Numerical study of nanoparticles aggregation on radiative 3D flow of maxwell fluid over a permeable stretching surface with thermal radiation and heat source/sink, *Results Eng.*, **19** (2023), 101208. https://doi.org/10.1016/j.rineng.2023.101208
27. T. Salahuddin, G. Fatima, M. Awais, M. Khan, B. Al Awan, Adaptation of nanofluids with magnetohydrodynamic Williamson fluid to enhance the thermal and solutal flow analysis with viscous dissipation: A numerical study, *Results Eng.*, **21** (2024), 101798. https://doi.org/10.1016/j.rineng.2024.101798
28. N. B. Khedher, Z. Ullah, Y. M. Mahrous, S. Dhahbi, S. Ahmad, H. Abu-Zinadah, et al., Viscous dissipation effect on amplitude and oscillating frequency of heat transfer and electromagnetic waves of magnetic driven fluid flow along the horizontal circular cylinder, *Case Stud. Therm. Eng.*, **55** (2024), 104142. https://doi.org/10.1016/j.csite.2024.104142
29. A. Rehman, M. C. Khun, A. S. Alsubaie, M. Inc, Influence of Marangoni convection, viscous dissipation, and variable fluid viscosity of nanofluid flow on stretching surface analytical analysis, *ZAMM-J. Appl. Math. Mech. Für Angew. Math. Und Mech.*, **104** (2024), e202300413. https://doi.org/10.1002/zamm.202300413
30. S. Akram, K. Saeed, M. Athar, A. Riaz, A. Razia, M. A. S. Al-Malki, Enhancing retention of biological fluid transport of magnetized thermal radiative pseudoplastic nanofluid with double diffusion convection, viscous dissipation and boundary slips, *Part. Sci. Technol.*, **43** (2025), 1–14. https://doi.org/10.1080/02726351.2024.2412654
31. S. Li, S. Akbar, M. Sohail, U. Nazir, A. Singh, M. Alanazi, et al., Influence of buoyancy and viscous dissipation effects on 3D magneto hydrodynamic viscous hybrid nano fluid ($MgO-TiO_2$) under slip conditions, *Case Stud. Therm. Eng.*, **49** (2023), 103281. https://doi.org/10.1016/j.csite.2023.103281
32. B. Alqahtani, E. R. El-Zahar, M. B. Riaz, L. F. Seddek, A. Ilyas, Z. Ullah, et al., Computational analysis of microgravity and viscous dissipation impact on periodical heat transfer of MHD fluid along porous radiative surface with thermal slip effects, *Case Stud. Therm. Eng.*, **60** (2024), 104641. https://doi.org/10.1016/j.csite.2024.104641
33. N. Abid, J. Hasnain, Viscous dissipation effects on the axisymmetric flow of Casson rheological fluid in the core region of curved artery surrounded by Al_2O_3/γ-Al_2O_3 nanofluid, *Int. J. Heat Fluid Flow.*, **107** (2024), 109349. https://doi.org/10.1016/j.ijheatfluidflow.2024.109349
34. M. Irfan, I. Siddique, K. A. Gepreel, M. Nazeer, D. Abduvalieva, M. I. Khan, Investigation of heat transfer phenomenon in a complex wavy divergent channel under the effects of thermal radiation, joule heating and electroosmosis, *Numer. Heat Tr. A-Appl.*, 2024, 1–20. https://doi.org/10.1080/10407782.2024.2386033
35. N. Elboughdiri, K. Javid, P. Lakshminarayana, A. Abbasi, Y. Benguerba, Effects of Joule heating and viscous dissipation on EMHD boundary layer rheology of viscoelastic fluid over an inclined plate, *Case Stud. Therm. Eng.*, **60** (2024), 104602. https://doi.org/10.1016/j.csite.2024.104602
36. N. Hasan, S. Saha, Effects of internal heat production and Joule heating on MHD conjugate mixed convection and entropy production inside a thermally non-homogeneous cooling system, *Ann. Nucl. Energy*, **206** (2024), 110671. https://doi.org/10.1016/j.anucene.2024.110671
37. E. Ghaderi, M. Bijarchi, S. K. Hannani, A. Nouri-Borujerdi, Evaluating Joule heating influence on heat transfer and entropy generation in MHD channel flow: A parametric study and ill-posed problem solution using PINNs, *arXiv preprint*, 2024. https://doi.org/10.48550/arXiv.2406.15810
38. A. Ullah, H. Yao, F. Ullah, W. Khan, H. Gul, F. A. Awwad, et al., Viscous dissipation and Joule heating effects on the unsteady micropolar fluid flow past a horizontal surface of revolution, *Alex. Eng. J.*, **94** (2024), 159–171. https://doi.org/10.1016/j.aej.2024.03.032

39. T. Abdeljawad, M. Sohail, D. R. Mostapha, Impacts of Hall current and Joule heating of Cattaneo-Christov on peristaltic stenosed artery of Reiner-Rivlin liquid through Darcy-Forchheimer feature, *Ain Shams Eng. J.*, **15** (2024), 102679. https://doi.org/10.1016/j.asej.2024.102679
40. A. Tahiri, H. Ragueb, M. Moussaoui, K. Mansouri, D. Guerraiche, K. Guerraiche, Heat transfer and entropy generation in viscous-joule heating MHD microchannels flow under asymmetric heating, *Int. J. Numer. Method. H.*, **34** (2024), 3953–3978. Available from: https://www.researchgate.net/publication/383332552.
41. H. Waqas, M. Imran, M. M. Bhatti, Bioconvection aspects in non-Newtonian three-dimensional Carreau nanofluid flow with Cattaneo–Christov model and activation energy, *Eur. Phys. J. Spec. Top.*, **230** (2021), 1317–1330. https://doi.org/10.1140/epjs/s11734-021-00046-8
42. T. Hayat, A. Aziz, T. Muhammad, A. Alsaedi, Numerical simulation for three-dimensional flow of Carreau nanofluid over a nonlinear stretching surface with convective heat and mass conditions, *J. Braz. Soc. Mech. Sci. Eng.*, **41** (2019), 1–11. https://doi.org/10.1007/S40430-018-1540-7
43. K. G. Kumar, G. K. Ramesh, B. J. Gireesha, R. S. R. Gorla, Characteristics of Joule heating and viscous dissipation on three-dimensional flow of Oldroyd B nanofluid with thermal radiation, *Alex. Eng. J.*, **57** (2018), 2139–2149. https://doi.org/10.1016/j.aej.2017.06.006
44. T. Muhammad, T. Hayat, S. A. Shehzad, A. Alsaedi, Viscous dissipation and Joule heating effects in MHD 3D flow with heat and mass fluxes, *Results Phys*., **8** (2018), 365–371. https://doi.org/10.1016/j.rinp.2017.12.047
45. P. Priyadharshini, M. V. Archana, N. A. Shah, M. H. Alshehri, Ternary hybrid nanofluid flow emerging on a symmetrically stretching sheet optimization with machine learning prediction scheme, *Symmetry*, **15** (2023), 1225. https://doi.org/10.3390/sym15061225
46. N. Acharya, S. Maity, P. K. Kundu, Framing the hydrothermal features of magnetized TiO_2–$CoFe_2O_4$ water-based steady hybrid nanofluid flow over a radiative revolving disk, *Multidiscip. Model. Ma.*, **16** (2020), 765–790. https://doi.org/10.1108/MMMS-08-2019-0151
47. K. A. M. Alharbi, A. E. S. Ahmed, M. O. Sidi, N. A. Ahammad, A. Mohamed, M. A. El-Shorbagy, et al., Computational valuation of Darcy ternary-hybrid nanofluid flow across an extending cylinder with induction effects, *Micromachines*, **13** (2022), 588. https://doi.org/10.3390/mi13040588
48. F. Wang, U. Nazir, M. Sohail, E. R. El-Zahar, C. Park, P. Thounthong, A Galerkin strategy for tri-hybridized mixture in ethylene glycol comprising variable diffusion and thermal conductivity using non-Fourier's theory, *Nanotechnol. Rev.*, **11** (2022), 834–845. https://doi.org/10.1515/ntrev-2022-0050
49. B. Unyong, R. Vadivel, M. Govindaraju, R. Anbuvithya, N. Gunasekaran, Entropy analysis for ethylene glycol hybrid nanofluid flow with elastic deformation, radiation, non-uniform heat generation/absorption, and inclined Lorentz force effects, *Case Stud. Therm. Eng.*, **30** (2022), 101639. https://doi.org/10.1016/j.csite.2021.101639
50. T. S. Kumar, Hybrid nanofluid slip flow and heat transfer over a stretching surface, *Part. Differ. Equ. Appl. Math.*, **4** (2021), 100070. https://doi.org/10.1016/j.padiff.2021.100070
51. F. Wang, E. O. Fatunmbi, A. T. Adeosun, S. O. Salawu, I. L. Animasaun, I. E. Sarris, Comparative analysis between copper ethylene-glycol and copper-iron oxide ethylene-glycol nanoparticles both experiencing Coriolis force, velocity and temperature jump, *Case Stud. Therm. Eng.*, **47** (2023), 103028. https://doi.org/10.1016/j.csite.2023.103028
52. T. A. Yusuf, F. Mabood, W. A. Khan, J. A. Gbadeyan, Irreversibility analysis of Cu-TiO_2-H_2O hybrid-nanofluid impinging on a 3-D stretching sheet in a porous medium with nonlinear radiation: Darcy-Forchhiemer's model, *Alex. Eng. J.*, **59** (2020), 5247–5261. https://doi.org/10.1016/j.aej.2020.09.053

53. F. Mabood, K. Das, Melting heat transfer on hydromagnetic flow of a nanofluid over a stretching sheet with radiation and second-order slip, *Eur. Phys. J. Plus.*, **131** (2016), 1–12. https://doi.org/10.1140/epjp/i2016-16003-1
54. L. Xu, E. W. M. Lee, Variational iteration method for the magnetohydrodynamic flow over a nonlinear stretching sheet, *Abstr. Appl. Anal.*, 2013, 573782. https://doi.org/10.1155/2013/573782

AIMS Press